

La investigación reportada en esta tesis es parte de los programas de investigación del CICESE (Centro de Investigación Científica y de Educación Superior de Ensenada, Baja California).

La investigación fue financiada por el CONAHCYT (Consejo Nacional de Humanidades, Ciencias y Tecnologías).

Todo el material contenido en esta tesis está protegido por la Ley Federal del Derecho de Autor (LFDA) de los Estados Unidos Mexicanos (México). El uso de imágenes, fragmentos de videos, y demás material que sea objeto de protección de los derechos de autor, será exclusivamente para fines educativos e informativos y deberá citar la fuente donde la obtuvo mencionando el autor o autores. Cualquier uso distinto como el lucro, reproducción, edición o modificación, será perseguido y sancionado por el respectivo o titular de los Derechos de Autor.

CICESE © 2023, Todos los Derechos Reservados, CICESE

# Centro de Investigación Científica y de Educación Superior de Ensenada, Baja California



---

## Maestría en Ciencias en Nanociencias

---

### First-principles calculations focused on the study of MXenes with potential applications in energy storage devices

Tesis

para cubrir parcialmente los requisitos necesarios para obtener el grado de  
Maestro en Ciencias

Presenta:

**Victor Hugo Medina Macias**

Ensenada, Baja California, México

2023

Tesis defendida por

**Victor Hugo Medina Macias**

y aprobada por el siguiente Comité

---

Dr. Rodrigo Ponce Pérez

Codirector de tesis

---

Dra. María Guadalupe Moreno Armenta

Codirectora de tesis

Dr. Eduardo Antonio Murillo Bracamontes

Dr. Héctor Noé Fernández Escamilla

Dr. Jassiel Rolando Rodríguez Barreras



---

Dra. Catalina López Bastidas

Coordinadora del Posgrado en Nanociencias

---

Dra. Ana Denise Re Araujo

Directora de Estudios de Posgrado

Resumen de la tesis que presenta Víctor Hugo Medina Macías como requisito parcial para la obtención del grado de Maestro en Ciencias en Nanociencias.

### **First-principles calculations focused on the study of MXenes with potential applications in energy storage devices**

Resumen aprobado por:

---

Dr. Rodrigo Ponce Pérez

Codirector de tesis

---

Dra. María Guadalupe Moreno Armenta

Codirectora de tesis

Mediante cálculos de primeros principios se ha demostrado la viabilidad del MXene formado por la aleación ordenada Ti/Ta como material anódico en baterías de iones de litio, esto debido a sus propiedades electroquímicas prometedoras. Sin embargo, la influencia de los grupos funcionales superficiales en el proceso atómico de litación permanecen desconocidos. En esta tesis, empleamos cálculos de primeros principios basados en la Teoría del Funcional de la Densidad (DFT) para investigar la estabilidad termodinámica, las características estructurales y las propiedades electroquímicas del MXene de aleación ordenada  $Ti_2Ta_2C_3$  funcionalizado con grupos O, F, Cl y OH, durante el proceso de intercalación de iones de litio. Nuestros cálculos demuestran la estabilidad termodinámica de la funcionalización superficial con grupos O, F, Cl y OH, indicando su viabilidad como grupos funcionales. Adicionalmente, identificamos el sitio de alta simetría H3 como la configuración más estable para la intercalación de Li. Para evaluar el rendimiento electroquímico, se realizó la caracterización electroquímica empleando curvas de voltaje de circuito abierto (OCV). Nuestros hallazgos demuestran cambios en la capacidad de almacenamiento dependiendo del grupo funcional, siendo el MXene funcionalizado con oxígenos el que exhibe mayores capacidades de almacenamiento en contraste con los otros grupos funcionales presentes en el MXene  $Ti_2Ta_2C_3$ . Las capacidades gravimétricas de almacenamiento para los ánodos de  $Ti_2Ta_2C_3$  de una sola capa funcionalizados con O, F y Cl son 91.77, 52.38 y 24.21 mAh/g, respectivamente. Los MXenes funcionalizados con grupos OH no mostraron estabilidad termodinámica durante el proceso de litación y favorecieron la formación de *clusters* de Li en su lugar. Estos resultados demuestran cómo los grupos funcionales cambian el rendimiento potencial de MXenes de  $Ti_2Ta_2C_3$  en aplicaciones de almacenamiento de energía y proporciona información para seleccionar correctamente el grupo funcional del material base.

**Palabras clave:** MXene, MXene de aleación ordenada, Bateria de Li-ion, Material anódico

Abstract of the thesis presented by Victor Hugo Medina Macias as a partial requirement to obtain the Master of Science degree in Nanoscience.

### **First-principles calculations focused on the study of MXenes with potential applications in energy storage devices**

Abstract approved by:

First-principles studies of Ti/Ta-based ordered alloy MXenes have demonstrated their viability as anode material in Li-ion batteries due to their promising electrochemical properties. However, the influence of surface functional groups on the atomic-scale lithiation processes remains unknown. In this thesis, we employ first-principles density functional theory (DFT) calculations to investigate the thermodynamic stability, structural characteristics, and electrochemical properties of O-, F-, Cl-, and OH-functionalized  $\text{Ti}_2\text{Ta}_2\text{C}_3$  ordered alloy MXenes during Li intercalation. Our calculations reveal surface functionalization with O, F, Cl, and OH is thermodynamically stable, indicating their viability as functional groups. Also, we identify the H3 high symmetry site as the most favorable configuration for Li intercalation. To evaluate electrochemical performance, electrochemical characterization is carried out employing open circuit voltage (OCV) curves. Our findings demonstrate changes in storage capacities depending on the functional group, with O-functionalized MXenes exhibiting larger storage capacities in contrast to other functional groups in  $\text{Ti}_2\text{Ta}_2\text{C}_3$  MXene anode materials. The theoretical single-layer gravimetric storage capacities for O-, F-, and Cl-functionalized  $\text{Ti}_2\text{Ta}_2\text{C}_3$  MXene anodes are 91.77, 52.38, and 24.21 mAh/g, respectively. OH-functionalized MXenes failed to show thermodynamic stability during lithiation and favored Li cluster formation over an intercalation process. These results show how functional groups affect the potential performance of  $\text{Ti}_2\text{Ta}_2\text{C}_3$  MXene materials in energy storage applications and provide insights for correctly selecting the functional group of the host material.

**Keywords: MXene, ordered alloy MXene, Li-ion battery, Anode material**

## **Dedication**

**This thesis is dedicated to my mother, Eva Macias, and my family.**

## Acknowledgements

I'd like to thank the *Centro de Investigación Científica y de Educación Superior de Ensenada* and the *Centro de Nanociencias y Nanotecnología* (UNAM) for giving me the chance to continue my academic career and for providing the resources to make this thesis possible.

Additionally, I want to thank the *Consejo Nacional de Humanidades, Ciencias y Tecnologías* (CONAH-CyT) for providing the financial support to make my post-graduate studies possible.

I want to thank DGAPA-UNAM for the financing provided through projects IN101523 and IA100624. The calculations were done in the supercomputing center DGTIC-UNAM through projects LANCAD-UNAM-DGTIC-150 and LANCAD-UNAM-DGTIC-422. I thankfully acknowledge the computer resources, technical expertise and support provided by the *Laboratorio Nacional de Supercómputo del Sureste de México*, CONAHCYT member of the network of national laboratories.

My sincere gratitude to my thesis advisor Dr. Rodrigo for being an excellent professor, friend, and advisor. His patience and guidance helped me overcome the challenges throughout the writing of this thesis and the research in it. It is my goal to become as skillful and knowledgeable as him someday.

I'd also like to thank my co-advisor, Dr. María Guadalupe, and the rest of my thesis committee for providing valuable feedback to improve the quality of my research and the content of this thesis.

I thank Dr. Jonathan Guerrero and the entire team at the *Laboratorio Virtual de Modelado de Materiales* for the weekly feedback meetings and general fun times. I thank Aldo Rodriguez and Israel Paez Ornelas for the technical support provided as well.

A big thank you to my friends in Ensenada, Mexico. Heriberto, Anahí, Sory, Carlos, Astrid, and so many others; without them, my post-graduate studies would not have had the spice that they did.

# Table of contents

	Page
Abstract in Spanish .....	ii
Abstract in English .....	iii
Dedication .....	iv
Acknowledgements .....	v
List of figures .....	viii
List of tables .....	ix
<b>Chapter 1 Introduction</b>	
1.1 Energy consumption and the need for renewable energies .....	1
1.2 Energy storage technologies .....	2
1.2.1 Li-ion battery electrode materials .....	4
1.3 Nanotechnology and 2D materials .....	4
1.4 MXene as Li-ion battery anode material .....	5
<b>Chapter 2 Literature Review</b>	
2.1 Overview of MXene structure, properties, and synthesis .....	6
2.2 The ordered-alloy titanium carbide MXene as Li-ion battery anode material .....	8
<b>Chapter 3 Hypothesis &amp; Objectives</b>	
3.1 Hypothesis .....	10
3.2 Objectives .....	10
3.2.1 General Objective .....	10
3.2.2 Specific Objectives .....	10
<b>Chapter 4 Methodology</b>	
4.1 Computational methodology .....	11
4.2 Methodology Theoretical Framework .....	12
4.2.1 Quantum mechanics in materials science .....	12
4.2.2 The Born-Oppenheimer Approximation .....	13
4.2.3 Hartee-Fock .....	13
4.2.4 Density Functional Theory .....	14
4.2.4.1 Electron density .....	14
4.2.4.2 Hohenberg-Kohn theorems .....	15
4.2.5 The Kohn-Sham approach to DFT .....	16
4.2.6 Exchange-correlation functional .....	18
4.2.6.1 Local density approximation .....	18
4.2.6.2 Generalized gradient approximation .....	18
4.2.7 Pseudopotentials .....	19
4.2.8 Surface Formation Energy Formalism .....	20
4.2.9 Open Circuit Voltage .....	21

<b>Chapter 5</b>	<b>Results &amp; Discussion</b>	
5.1	MAX-phase . . . . .	22
5.1.1	Optimization . . . . .	23
5.2	MXene . . . . .	24
5.2.1	Ti <sub>4</sub> C <sub>3</sub> . . . . .	24
5.2.2	Ti <sub>2</sub> Ta <sub>2</sub> C <sub>3</sub> . . . . .	25
5.2.3	Ti <sub>2</sub> Ta <sub>2</sub> C <sub>3</sub> T <sub>z</sub> . . . . .	25
5.3	2x2 Supercell . . . . .	26
5.3.1	Crystal lattice optimization . . . . .	27
5.3.2	Thermodynamic stability of Ti <sub>2</sub> Ta <sub>2</sub> C <sub>3</sub> T <sub>z</sub> MXenes . . . . .	28
5.3.3	Electronic Properties . . . . .	29
5.3.3.1	Band structure . . . . .	29
5.3.3.2	Electrostatic potential isosurfaces . . . . .	31
5.4	Lithiated MXenes . . . . .	31
5.4.1	Description of the lithiation process on the cell surface . . . . .	31
5.4.2	Thermodynamic stability of the lithiated MXenes . . . . .	33
5.4.3	Electrochemical characterization: open-circuit voltages . . . . .	33
5.4.4	Li-ion diffusion paths . . . . .	36
<b>Chapter 6</b>	<b>Conclusion</b>	
<b>References</b>		39

## List of figures

Figure	Page
1 ESTs classified by storage mechanism. . . . .	2
2 Basic schematic of a secondary battery. . . . .	3
3 Illustration showcasing the "smoothing" of the wave function and its corresponding potential, also called the pseudopotential, in comparison to an all-electron (AE) wave function. Graph borrowed from June Gunn Lee's book "Computational Materials Science: An Introduction" (2000) Henkelman et al. (2016) Lee Henkelman et al. (2000). . . . .	19
4 $Ti_4AlN_3$ to $Ti_4AlC_3$ . . . . .	22
5 Optimization plots for $Ti_4AlC_3$ : a) cutoff energy, b) k-points (x-x-1), c) k-points (10-10-x), and d) lattice parameter. . . . .	22
6 Schema showing how the $Ti_2Ta_2C_3T_z$ MXene was built from a MAX-phase $Ti_4AlC_3$ starting point. Ti, Al, Ta, and C are represented by the blue, livid, yellow, and brown spheres, respectively. . . . .	24
7 $Ti_4C_3$ lattice parameter optimization. . . . .	25
8 $Ti_2Ta_2C_3$ lattice parameter optimization. . . . .	25
9 Top view of a $Ti_2Ta_2C_3$ unit cell showing the positions of the four high-symmetry sites. . . . .	26
10 Transformation of a $Ti_2Ta_2C_3$ formula unit cell into a 2x2 $Ti_2Ta_2C_3$ supercell. . . . .	27
11 Band structures for 11a) $Ti_2Ta_2C_3$ , 11b) $Ti_2Ta_2C_3O_2-Br$ , 11c) $Ti_2Ta_2C_3F_2-H3$ , 11d) $Ti_2Ta_2C_3Cl_2-T4$ , and 11e) $Ti_2Ta_2C_3(OH)_2-Top$ . . . . .	30
12 Electrostatic potential isosurfaces for O-, F-, Cl-, and OH-functionalized $Ti_2Ta_2C_3$ MXenes in the H3 high-symmetry site in top view. . . . .	31
13 $Ti_2Ta_2C_3Li$ unit cell top view displaying the Li adatom in four high-symmetry sites: a) Bridge, b) H3, c) T4, and d) Top. All four variants use a base H3 high-symmetry site for the functional group. . . . .	32
14 Open circuit voltage curves for the functionalized $Ti_2Ta_2C_3T_z$ MXenes. Maximum Li capacity is observed when OCV = 0. Positive OCV values show Li intercalation, while negative values indicate surface cluster formation. . . . .	35
15 Minimum energy pathways for a) $Ti_2Ta_2C_3O_2Li$ and b) $Ti_2Ta_2C_3O_2Li$ . In the oxidized MXene, the Li adatom travels from H3 to H3 site, with a saddle point at T4 and an energy barrier of around 0.36 eV. In the fluorinated MXene, Li travels from H3 to H3, with a metastable site at T4 (0.28 eV) and saddle points (0.26 eV) at the bridge site. . . . .	36
16 Atomic visual models for the Li diffusion process over the surface of the functionalized MXenes. . . . .	36

## List of tables

Table		Page
1	Functionalized MXene lattice parameter in Å compared to pristine $Ti_2Ta_2C_3$ . In pristine form, no functional group is considered. . . . .	26
2	Functionalized 2x2 supercell MXene lattice parameter in Å. . . . .	27
3	Functionalized 2x2 supercell MXene relative energies in eV. . . . .	28
4	Surface formation energy results for the most stable high-symmetry site of each group. . . . .	29
5	Relative energies (eV) for the lithiated MXene at various lithium concentrations per formula unit cell. . . . .	32
6	SFE (eV) of the lithiated MXenes as the lithium concentration increases per formula unit cell. . . . .	33
7	Theoretical gravimetric capacities calculated from the maximum Li capacity for each MXene anode material. . . . .	35

# Chapter 1. Introduction

---

## 1.1 Energy consumption and the need for renewable energies

Energy consumption worldwide has increased sharply since the invention of the light bulb in the 19th century. There is no indication that energy consumption will reach a plateau soon. The U.S. Energy Information Administration (EIA) estimates (2021) that by the year 2050, global energy expenditure will increase by nearly 50% compared to the total expenditure of 2020. The energy consumed globally comes from a diverse set of sources that generate energy according to the needs of their respective consumers. The EIA measured a total energy output of 85% for non-renewable energy sources (coal, petroleum and other liquids, natural gas, and nuclear), while renewable energy sources only produced 15% of the total energy consumed worldwide in 2020. By 2050, renewable energy consumption is expected to increase to 27%, while non-renewable energy consumption will decrease accordingly. The primary driver of the increase in the consumption of renewable energy sources is electrical energy, which grew in total energy produced from renewable sources by 3% from 2019 to 2020 (International Energy Agency, 2021).

In Mexico, the *Secretaría de Energía* (Secretaría de Energía, 2016) reported that energy production depends heavily on non-renewable resources. Non-renewable energy sources generated 88.75% of the total energy consumed in Mexico during 2020, while renewable sources supplied the remaining 11.25%. The report also included a perspective of renewable energies where it detailed a strategy of increasing the production of clean energy to 37.5% by 2030 and 50% by 2050.

The technological shift from non-renewable to renewable energy plays a key role in combating climate change. As the transition to renewable energy progresses, arduous challenges preventing widespread adoption must be overcome. They are targets to meet world governments' goals for prospective renewable energy demand, including Mexico.

The driver for the increase in renewable energy adoption is electrical energy. Currently, there are two primary sources for the production of clean electrical energy (Stram, 2016): wind and solar. For non-renewable energies, electrical energy is produced to meet the demands of its consumption. On the other hand, renewable energy sources may not always provide enough electrical energy to meet consumption demands. Solar power depends on the availability of the sun, and wind energy depends on the availability of strong winds. Both of these sources are dynamic and vary depending on diverse factors.

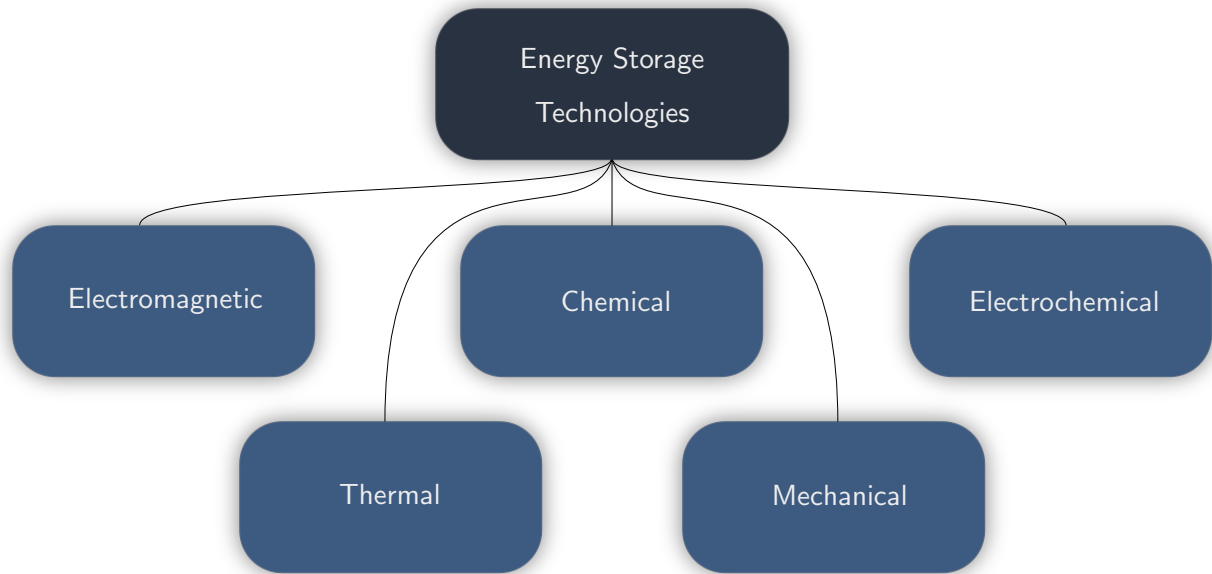


Figure 1. ESTs classified by storage mechanism.

## 1.2 Energy storage technologies

Although renewable electrical energy production may not always meet consumption demands, its consumption may not always exceed production, resulting in excess energy available to be stored. Several energy storage technologies (ESTs) can be classified according to their storage mechanism (Tan et al., 2021), figure 1 gives a brief overview of the different ESTs classified by their type of storage mechanism. Each EST has specific features and advantages that are key to its utilization over other types of storage technologies depending on the field of application. Electrochemical ESTs (eESTs) are of particular research interest due to their widespread utilization in storing electrical energy for portable devices (consumer electronics, electric vehicles, and military technologies, among others.). Additionally, compared to other ESTs, eESTs offer better efficiencies and scalability (Cho et al., 2015), which further supports their dominance in portable technology applications.

Traditionally, eESTs can be further classified into two subcategories: capacitors and batteries. These eESTs have important applications in storing electrical energy, but batteries stand out due to their longer charge/discharge rates and higher energy densities than capacitors (Martins et al., 2020). Disposable single-use batteries are known as primary batteries, while rechargeable batteries are known as secondary batteries. Secondary batteries are already a dominant choice in portable electronic devices. However, their further adoption to meet the increasing energy storage demands requires a cost-effective approach to building efficient and durable devices.

Secondary batteries are composed of four fundamental components: an anode and a cathode (also known as electrodes), an ionic conducting medium known as an electrolyte, and a separator. Figure 2 shows a basic schematic of the standard battery structure. In these devices, electrical energy is stored as chemical energy due to a process of faradaic redox reactions. To store energy, an electric potential is applied at the electrodes causing ions suspended in the electrolyte to move from one electrode to the other. The ions undergo intercalation, a term that describes a reversible process of insertion of a species into a layered structure (electrode), at the anode site and become reduced. To use the stored energy, that is, to discharge the battery, a load is applied, introducing a potential in the opposite direction of the charging state, causing the ions to oxidize and travel from the anode -in which they were previously intercalated- to the cathode. The electronic charge is carried from one electrode to the other by conducting current collectors to complete an electronic circuit when a load is applied to the battery. The performance of the battery heavily depends on the properties of the electrodes, including their ability to allow the intercalation of ions without suffering structural defects and other adverse effects (Julien et al., 2015).

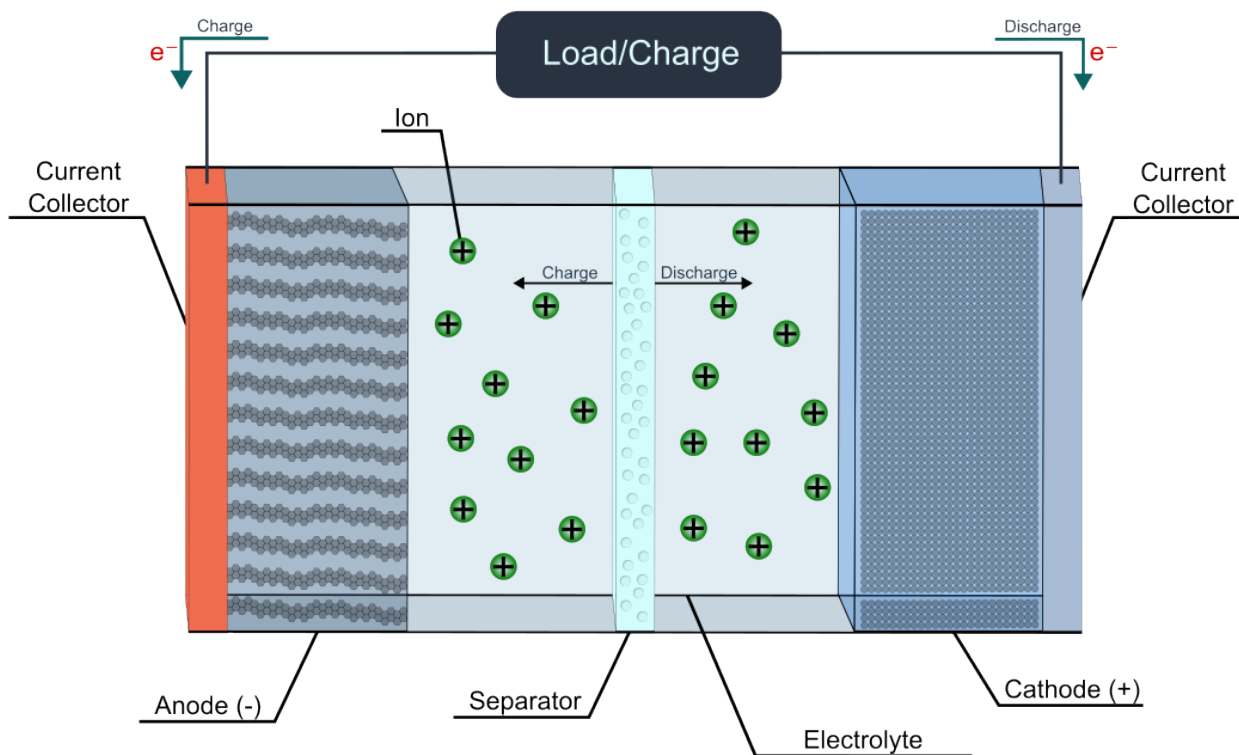


Figure 2. Basic schematic of a secondary battery.

Several types of secondary batteries can be found on the market. They are selected based on several factors such as associated costs, electrolyte mediums and associated ions, and electrode materials. Batteries based on lead-acid, nickel-cadmium, nickel-metal hydride, sodium-sulfur, lithium-ion (Li-ion),

and other types of materials (Energy Storage Association, 2022; Liang et al., 2019) are commercially available. Li-ion batteries stand out due to high volumetric and gravimetric densities, relative stabilities, long life cycles, and high output power (Deng, 2015; Zhu et al., 2017). These properties and characteristics have caused Li-ion batteries to dominate the rechargeable portable battery market, being found in everyday electronic devices such as smartphones and laptops, becoming the leading battery technology used in electric vehicles (Miao et al., 2019).

### **1.2.1 Li-ion battery electrode materials**

Li-ion battery electrode materials are chosen based on their ability to allow the intercalation of lithium (Li) ions without suffering large and permanent structural deformations due to mechanical strain that can damage the cell and reduce the battery performance. Cathode materials are made of open-structure layered compounds with a close-packed lattice of anions (Liu & Xue, 2010); every other space between the layers is filled with transition metals, leaving alternating empty layers where Li ions can intercalate and be stored. Anode materials are chosen based on their electrochemical potentials relative to the corresponding cathode material (Poulomi & Srivastava, 2014) and their ability to intercalate Li ions. Although Li was the first choice for anode material due to its high energy density, a property consequence of being the most electropositive metal, its use presented problems that needed to be solved. Anode corrosion occurred, leading to dendrite formation, lowering its charge-discharge life cycle span, which can lead to a potentially hazardous situation if the battery is exposed to the environment (Roselin et al., 2019). Three categories of anode materials serve as a replacement for Li anodes (Liu & Xue, 2010): 1) insertion-type materials, which include commonly used titanium (Ti) (e.g.,  $\text{Li}_4\text{Ti}_5\text{O}_{12}$  and  $\text{TiO}_2$ ) and carbon-based anodes (e.g., graphite, graphene), 2) conversion type materials (metal oxides), and 3) alloying-type materials (e.g., Si, Sn, Ge). Tackling anode materials can lead to better, more efficient Li-ion batteries to meet the increasing demand for clean-sourced electrical energy storage.

### **1.3 Nanotechnology and 2D materials**

Nanoscience and nanotechnology allow us to work with novel materials with dimensions on the nanometric scale to improve the already existing technology. Nanostructured materials are those with at least one dimension below 100 nm. In that sense, two-dimensional (2D) nanomaterials are those with two dimensions above the 100 nm threshold. 2D nanomaterials are sheet-like, and their thickness is usually below 5 nm in length (Hu et al., 2019); they can be as thin as one or a few atoms in length. 2D nanomaterials are an exciting prospect for Li-ion battery anode materials due to their tunable electrical

conductivity, specific surface area, and high mechanical strength (Aghamohammadi et al., 2022). The earliest observations of 2D materials are of graphene, or single sheets of graphite (Meyer et al., 2007). Graphene is made of a single-layer hexagonal structure with carbon atoms at the vertices of the hexagon. Excellent mechanical strength and electrical conductivity make graphene a well-suited electrode, precisely anode material. However, side reactions (e.g., electrolyte and functional group decomposition) prevent its adoption as the go-to anode material for Li-ion batteries (Lochala et al., 2017).

#### 1.4 MXene as Li-ion battery anode material

MXenes are a family of two-dimensional transition metal carbide and nitride materials that have previously been proposed as novel anode materials in Li-ion batteries (Sun et al., 2018). They have a general chemical formula of  $M_{n+1}X_nT_x$  where M is the early transition metal(s), X is the carbon or nitrogen atoms, and  $T_x$  is the surface termination (functional groups) along the main 2D nanostructure with  $n = 1 - 4$ . These 2D materials are highly regarded and studied in diverse scientific communities with various applications, most notably electrochemistry, due to their tunable chemical, electrical, and mechanical properties (Li et al., 2022). Notably, MXene materials with  $Ti_xTa_{(4-x)}C_3$  structure have previously been reported (Syamsai et al., 2021; Maldonado-Lopez et al., 2022) as candidate anode materials for Li-ion batteries. Syamsai et al. (2021) reported experimental anode  $Ti_xTa_{(4-x)}C_3$  MXenes with an expanded interlayer spacing allowing for effective Li-ion storage. They measured a high specific discharge capacity and exceptional reversible intercalation of Li ions, attributing the excellent performance of the MXene anode to a stable bi-metallic structure where ions can be stored on the surface of its layers. Additionally, Maldonado-Lopez et al. (2022) ran first-principles studies of the lithiation process of  $Ti_2Ta_2C_3$  MXenes compared to  $Ti_4C_3$  MXenes; they found that the titanium-tantalum structure allowed four times the storage of Li ions compared to the non-titanium structure. They demonstrated, computationally, the stability of  $Ti_2Ta_2C_3$  MXenes as Li-ion battery anode material and proposed future studies on the subject focus on functional groups (specifically, fluoridation and oxidation) attached to the structure to get a better outlook on its properties and potential application in Li-ion batteries. Thus, the importance of studying functionalized ordered-alloy  $Ti_xTa_{(4-x)}C_3$  MXenes along with its lithiation process is evident and gives purpose to this study.

## Chapter 2. Literature Review

---

### 2.1 Overview of MXene structure, properties, and synthesis

Before discussing MXenes, it becomes necessary to look at their origins beforehand. MXenes have the general chemical formula  $M_{n+1}X_nT_x$ . This family of novel materials was discovered in 2011 by Michael Naguib et al. The MXene was made by modifying a raw MAX phase material where similarly, M is the early transition metal and X is a carbon or nitrogen atom. A is typically an A-group element (primarily elements from the IIIA and IVA groups) that fills the space between the layered MXenes. MAX phase materials, in turn, have the general chemical formula  $M_{n+1}AX_n$  and were first described as “MAX phase” in the year 2000 by Michel W. Barsoum in an article published in the journal Progress in Solid State Chemistry. The article, titled “The  $M_{n+1}AX_n$  Phases: A New Class of Solids: Thermodynamically Stable Nanolaminates”, was the first detailed report on MAX phase materials, compiling a brief history of the first  $M_2AX$  class materials and subsequently on  $M_3AX_2$  class materials. Barsoum noted that the first reported MAX phase materials were published by Nowotny and his group in the sixties in a review article summarizing the work they had done over previous years synthesizing and documenting many carbides and nitride materials. Not all of them were what we would later call MAX phase materials, but they reported more than 30  $M_2AX$  phase materials which they called Hägg or H-phase materials. Then, in 1967, Nowotny and his group (?) discovered and published their work on  $Ti_3SiC_2$  and  $Ti_3GeC_2$ , a class of materials similar to H-phase materials - an A-element layer separated layers of hexagonal  $M_3X_2$  instead of  $M_2X$  layers. This work was followed up by Pietzka and Schuster in the early '90s adding  $Ti_3AlN_2$  to the list of  $M_3X_2$  class materials. Around the time that Barsoum's group published their first detailed report on MAX phase materials, they had also recently identified  $Ti_4AlN_3$ , which led them to conclude that there exist ternary layered materials with  $M_{n+1}AX_n$  phases, where n was reportedly 1, 2, and 3. The discovery and description of MAX phase materials were imperative to developing MXenes.

The first MXene was described in 2011, and the term “MXene” was coined in reference to its graphene-like morphology. Michael Naguib et al. (2011), in their article “Two-Dimensional Nanocrystals Produced by Exfoliation of  $Ti_3AlC_2$ ”, reported on bidimensional nanosheets composed of  $Ti_3C_2$  layers and conical scrolls synthesized by room temperature exfoliation of  $Ti_3AlC_2$  in hydrofluoric acid (HF).  $Ti_3AlC_2$  was treated in HF, in which the Al atoms interleaved between the MX layers were removed and replaced with OH functional groups. Using sonication in a methanol solution, the hydrogen bonds that bonded the OH groups, and therefore the MX layers, were broken, leading to the separation of the resulting nanosheets. A series of chemical characterization techniques confirmed the existence of

$\text{Ti}_3\text{C}_2(\text{OH})_2$ . Additionally, the geometry of simulated hydroxylated and fluorinated MXene layers was optimized using DFT-based calculations whereby the theoretical X-Ray diffraction (XRD) patterns of the optimized structures were compared to experimental XRD patterns. The computational and experimental results for were shown to be in good agreement, providing strong evidence for the formation of the hydroxylated MXene material. Treated powders of the MXene material showed good conductivity and ductility properties, along with the possibility of a tunable band gap through surface termination dopants (functional groups attached to the surface of the MXenes layers), allowing for potential electronic applications such as use in Li-ion batteries. In addition to the previous properties, the article's authors found that the exfoliated MXene material maintained the pseudoductility of the MAX phase  $\text{Ti}_3\text{AlC}_2$  and could be easily pressed into disk-shaped objects that served as electrode material for Li-ion batteries. The authors also proposed the layered structure of the synthesized MXene material as hosts for Li storage, including further DFT calculations without temperature and in a Li-rich environment to show the intercalation of the Li atoms in spaces that were previously occupied by the Al atoms of the former MAX phase material. The modeled  $\text{Ti}_3\text{C}_2\text{Li}_2$  electrode would provide a specific charge capacity of 320 mAh/g, which is comparable to the 372 mAh/g capacity of graphite in  $\text{LiC}_6$ . Naguib's DFT calculations found that the electronic properties of the MXene layers are in function of the surface terminations with band structures that resemble a semimetal. When the surface terminations are of OH and F functional groups, for example, it was found that the band structure presented band gaps of  $E_g = 0.05$  eV and  $E_g = 0.1$  eV, respectively. It is advantageous for electronic applications to be able to tune the band gap of the MXene material as it allows for a wide range of implementations in electronic devices.

The development of titanium-based carbide MXenes has been a steady growth field, experimentally demonstrating how surface termination functional groups influence the electrochemical properties of MXenes. In 2017, W. Sun et al., for the first time, showed that  $\text{Ti}_2\text{CT}_x$  MXenes could be synthesized via electrochemical etching of in a hydrochloric acid (HCl) aqueous solution. The bonding of the M-A group is much weaker than that of the M-X group; therefore, chemical etching can be used to remove Al atoms from the MAX phase  $\text{Ti}_2\text{AlC}$  structure selectively. Etching is usually done using hazardous HF or  $\text{LiF}/\text{HCl}$ ; Sun and his group instead utilized HCl, allowing for the formation of surface termination O, OH, and Cl functional groups (excluding F functional groups that were formed from the fluorine-heavy environment of HF). It was found that electrochemical performance was improved by introducing Cl functional groups into the surface terminations of the 2D nanosheets. This improvement was attributed to a larger d-spacing allowing for easier intercalation of ions, a promising prospect for potential Li-ion electrode applications.

## 2.2 The ordered-alloy titanium carbide MXene as Li-ion battery anode material

So far, MXenes seem to be a promising 2D material for electronic applications, with a single early transition metal atom filling the role of the M part of the MXene. However, Ryavuri Syamsai et al. (2021) reported on a bi-metallic MXene with titanium and tantalum transition metal atoms jointly taking on the role of the M atom in the MXene. According to the authors, titanium carbide MXenes are the most published MXene materials, and tantalum carbide structures have been gaining attention in electronic applications, hence the use of a titanium-tantalum carbide MXene as anode material for Li-ion batteries owing to its unique set of synergistic electrochemical properties. They report on the synthesis of bi-metallic  $Ti_xTa_{(4-x)}C_3$  (specifically for  $x = 2$ ) MXene with expanded interlayer spacing. When Ti and Ta form an alloy compound, Ti atoms will seek to occupy the outer layer of the structure while Ta will seek to settle in the middle layer. Ta has a natural self-oxidizing nature allowing for interesting physicochemical properties of the MXene material. The  $Ti_2Ta_2C_3$  MXene was synthesized through an etching process of a  $Ti_2Ta_2AlC_3$  MAX phase material in an aqueous HF solution which allowed for the removal of the A-group atom from the nanostructure. A series of chemical and electrochemical characterization techniques were applied to the bi-metallic MXene to confirm its chemical composition and function as anode material for Li-ion batteries. The layered  $Ti_2Ta_2C_3$  MXenes displayed an interlayer d-spacing of 3.37 Å, allowing for the intercalation of Li ions between the MX layers. Furthermore, Syamsai reported a remarkably high specific discharge capacity of about 459 mAh/g at an applied C-rate of 0.5 C (the measured specific capacity should be supplied at a discharge time of two hours) with an excellent Coulombic efficiency of around 99% after 200 cycles. These properties of the tantalum-carbide bi-metallic MXene further support the potential application of MXenes as electrode materials, specifically anode materials, for Li-ion batteries. A further step would be to functionalize these ordered alloy MXenes with surface terminations to measure their effects on the performance of the anode material.

Syamsai's work demonstrated experimentally that  $Ti_xTa_{(4-x)}C_3$  is capable of being applied as a high-capacity anode material. However, the lithiation process was not understood until early 2022, when Daniel Maldonado-Lopez et al. published a detailed article studying the lithiation process of  $Ti_4C_3$  and  $Ti_xTa_{(4-x)}C_3$  through experimental and theoretical methods. It is not possible to understand the lithiation process in these MXene materials by experimental electrochemical means, such as potentiostatic or galvanostatic analysis. Therefore, their work was accompanied by DFT calculations to get a clearer picture of the process of storing Li ions and the structural stability of the MXene materials. Their experimental results show that  $Ti_2Ta_2C_3$  has a specific discharge capacity of 477 mAh/g with a Coulombic efficiency of 99% at a C-rate of 0.25 (4 h) after 100 cycles.  $Ti_4C_3$ , in comparison, displayed a discharge

capacity of 239 mAh/g under the same conditions. Furthermore, the  $\text{Ti}_2\text{Ta}_2\text{C}_3$  structure was found to store 8.8 moles of Li/mol of active material. The bi-metallic MXene stored four times more Li ions than the mono-metallic MXene. They also observed that as the number of charge-discharge cycles increased, there was a moderate increase in the capacity of the bi-metallic MXene. A possible explanation is the expansion of the interlayer distance upon cycling due to the natural characteristics of the crystal material (such as defects, functionalization, and particle size).

In their computational analysis, they first studied the lithiation process of  $\text{Ti}_4\text{C}_3$  MXene materials. They found that the system energy was much higher in interstitial and substitutional Li atoms compared to Li adatoms, suggesting that adatom lithiation was the primary intercalation method of Li ions in MXene materials. Subsequent studies of the lithiation process in  $\text{Ti}_x\text{Ta}_{(4-x)}\text{C}_3$  MXenes were done solely with adatom lithiation. Systematic doping of  $\text{Ti}_4\text{C}_3$  with Ta atoms in different lattice positions allowed for the study of several atomic Ti/Ta structural configurations; the most stable atomic configuration was found to be the 50%/50% Ti/Ta (with Ta atoms located in the innermost MXene layers) further supporting previous work done with  $\text{Ti}_2\text{Ta}_2\text{C}_3$  materials. Additionally,  $\text{Ti}_2\text{Ta}_2\text{C}_3$  was found stable in a wide range of chemical potentials. At the same time,  $\text{Ti}_4\text{C}_3$  failed to show the stability range of the former material operating on a narrower chemical potential. Their results, along with the previous work done by Syamsai, showed that  $\text{Ti}_2\text{Ta}_2\text{C}_3$  is a superior MXene candidate for anode material in secondary Li-ion batteries.

To deepen the understanding of the potential use of  $\text{Ti}_2\text{Ta}_2\text{C}_3$  in energy storage devices, Maldonado suggests further studies focus on the effect of the functional group (O, F, Cl, and OH) on the  $\text{Ti}_2\text{Ta}_2\text{C}_3$  MXene. No known studies have been published that study the impact of functional groups on  $\text{Ti}_x\text{Ta}_{(4-x)}\text{C}_3$  and their performance as Li-ion battery anode material.

## Chapter 3. Hypothesis & Objectives

---

### 3.1 Hypothesis

The surface functionalization of Ti-based ordered-alloy carbide MXenes  $\text{Ti}_x\text{Ta}_{(4-x)}\text{C}_3$  functionalized with O, OH, Cl, and F functional groups will modify lithium ion diffusion paths and intercalation processes compared to the pristine MXene.

### 3.2 Objectives

#### 3.2.1 General Objective

Study the lithiation process of functionalized Ti-based ordered alloy MXene materials using first-principles total-energy calculations based on the DFT framework.

#### 3.2.2 Specific Objectives

- Optimize the structural parameters of functionalized  $\text{Ti}_x\text{Ta}_{(4-x)}\text{C}_3$  MXene materials using DFT as implemented in the Vienna Ab-initio Simulation Package (VASP).
- Study the electronic and structural properties of functionalized Ti-based MXenes.
- Describe the electrochemical properties of the functionalized  $\text{Ti}_x\text{Ta}_{(4-x)}\text{C}_3$  materials.
- Using the Nudged Elastic Band (NEB) method, study the lithiation process of functionalized  $\text{Ti}_x\text{Ta}_{(4-x)}\text{C}_3$  MXene surfaces.
- Describe the most probable and stable ion diffusion paths and ion intercalation processes on the MXene surface.
- Describe the effects of the O, F, Cl, and OH functional groups on the lithium storage capacity of  $\text{Ti}_x\text{Ta}_{(4-x)}\text{C}_3$  MXene surfaces.
- Propose the best candidate among the functionalized  $\text{Ti}_x\text{Ta}_{(4-x)}\text{C}_3$  MXene materials for Li-ion battery applications.

## Chapter 4. Methodology

---

### 4.1 Computational methodology

First-principles calculations were performed using the VASP software package, employing the DFT framework to study the structural and electronic properties of the ordered-alloy  $\text{Ti}_2\text{Ta}_2\text{C}_3\text{T}_z$  MXene. The projector-augmented wave (PAW) pseudopotentials were employed to describe the interaction between electrons and ions. For the exchange-correlation functional, we utilized the general gradient approximation (GGA) described by Perdew, Burke, and Ernzerhof (PBE) ((Perdew et al., 1996)). The functionalized MXene materials were built by modifying pre-existing MAX-phase structure files obtained from The Materials Project using the VESTA 3D visualization software (Momma & Izumi, 2011). Further preprocessing and preparation of the input files were performed using the VASPKIT software package (Wang et al., 2021). The resulting ordered-alloy MXene structures underwent structural relaxation considering three structural parameters:

1. The cutoff energy for the plane wave basis.
2. The k-point grid employed to sample the first Brillouin zone.
3. The crystal lattice geometry confined to the **a** and **b** lattice parameters.

The convergence criterion for all self-consistent calculations was set to  $1 \times 10^{-4}$  eV; for the structural convergence, all force components must be less than 0.01 eV/Å. Van der Waals dispersion corrections were employed using the DFT-D3 method of Grimme (Grimme et al., 2010) with a zero-damping function. We made use of Fermi smearing to determine how the partial occupancies are set for each wavefunction with a smearing value of 0.2 eV. The postprocessing of the single-point field calculations was performed using a mixture of software packages, most notably VASPKIT, Origin Pro, GnuPlot, PyProcar, and others. Ion diffusion paths and intercalation processes between two stable lithiated states were studied employing the VASP Transition State Tools (Henkelman et al., 2000), notably, the Nudged Elastic Band calculation method offered by the tools package, a method for finding saddle points and minimum energy paths between two known stable states. The electrochemical properties of the materials were evaluated using open-circuit voltage (OCV) profiles as a function of the number of ion species present in the surface material.

To carry out our simulations, we made use of the compute resources offered by the MIZTLI super-computer of the (*Universidad Nacional Autónoma de México, UNAM*). Additionally, further computing resources were provided by the LAMB computing cluster of the (*Centro de Investigación Científica y de Estudios Superiores de Ensenada, CICESE*).

## 4.2 Methodology Theoretical Framework

### 4.2.1 Quantum mechanics in materials science

Material science deals with the research and engineering of materials; the basis for this research is chemistry and physics which governs matter and explains its behavior. First-principles material science methods seek to explain how matter behaves from no known experimental data. We must use the basic laws of physics to explain how matter behaves, its properties, and its characteristics. First-principles materials science often involves extremely small structures with dimensions at the nanoscale. Solving how its constituent matter, the electrons and nuclei that form its atoms, behave gives us descriptions of how the atoms themselves should behave as well. However, classical Newtonian physics breaks down when dealing with extremely small objects and structures and fails to accurately explain their behavior. On the other hand, quantum mechanics offers solutions that properly deal with this issue. Quantum mechanics is the physics of extremely small structures, at the scale of subatomic particles and atoms. Therefore, first-principles material science uses quantum mechanics as the basis for its calculations.

Following the wave nature of matter in quantum mechanics, we use the Schrödinger equation to explain how electrons behave in an atom. The simplified version of the time-independent Schrödinger equation is:

$$\hat{H}\Psi = E\Psi \quad (1)$$

where  $\Psi$  and  $E$  are the wave function and system energy value, respectively, and  $\hat{H}$  is the Hamiltonian operator of the system. This operator is the sum of all energies involved in the system, the kinetic and potential energies of the constituent particle waves, and their interactions with each other. It can be simplified to:

$$\hat{H} = -\frac{\hbar^2}{2m}\nabla^2 + V(r) \quad (2)$$

where  $-\frac{\hbar^2}{2m}$  represents the kinetic energy of the system and  $V(r)$  its potential energy. Here,  $\nabla^2$  is the Laplacian operator  $\frac{\partial^2}{\partial x^2} + \frac{\partial^2}{\partial y^2} + \frac{\partial^2}{\partial z^2}$ . The Hamiltonian operator acts upon the wave function to give its energy  $E\Psi$ . Note that the energy is quantized into energy levels and is a constant called the eigenvalue. We are only interested in the ground-state energy eigenvalue as it describes the properties of the ground-state system (material).

The differential equation that is the Schrödinger equation is easily solvable for the hydrogen atom, whose nucleus is made up of a single proton and has one sole electron orbiting it. The equation becomes very complex when dealing with larger atoms, however, and is not easily solvable even with the computational power offered in modern times. Its solution is practically impossible, so approximations were made that allowed researchers to solve the equation for many-body systems. These approximations are accurate enough to obtain a description of the properties of materials.

#### 4.2.2 The Born-Oppenheimer Approximation

The Hamiltonian operator, seen in simplified form in equation 2, includes all interactions between the constituent particles in a molecular system. The Hamiltonian includes energies for electron-electron, electron-nuclei, and nuclei-nuclei interactions; for many body systems, this leads to the increased complexity of solving the Schrödinger equation making it practically impossible to find solutions. However, because the nuclei of atoms are many orders of magnitude more massive than electrons (protons and neutrons are about 1800 times more massive than an electron), it is convenient to treat the nuclei as fixed particles. This is called the Born-Oppenheimer approximation. This model treats electrons as moving particles in a field of fixed nuclei. Recall from 2, the kinetic energy term includes an inverse mass term; in the Born-Oppenheimer approximation, since the nuclei are many orders of magnitude more massive than electrons, this term effectively becomes zero for nuclear interactions. Additionally, in a field of fixed nuclei, the nucleus-nucleus repulsion effect becomes a constant. This approximation helps simplify the Hamiltonian for many-body molecular systems to obtain a term that is more feasible to find solutions for.

#### 4.2.3 Hartee-Fock

In an attempt to reduce the complexity of the Schrödinger equation for many-body systems, the Hartree method treats electron interactions not independently but as a mean field. This also introduced the self-consistent field method for solving the Schrödinger wave equations, which treats an n-electron system as an average electron density. This method proved accurate results for the hydrogen atom but

gave only crude estimates for atoms with a larger number of electrons. In particular, it failed to consider the antisymmetry of the wavefunctions and exchange/correlation energies found in n-electron systems.

The Hartree-Fock (HF) method aimed to improve the accuracy of the Hartree method by acting on the wavefunction instead of the Hamiltonian. The wave function is treated as a linear combination of electron wavefunctions in a Slater determinant. In a Slater determinant, changing the coordinates of any two electrons changes the sign of the wavefunction guaranteeing antisymmetry. This method also introduces exchange energy: when two electron indices in a wavefunction are "exchanged" it also changes the sign of the wavefunction. This exchange energy is removed from the total energy expression from the Hartree method, which had a habit of overestimating the total energy, moving closer to observed values.

#### 4.2.4 Density Functional Theory

The Hartree-Fock method improved calculation times and offered accurate results, but it was still limited to systems with only tens of constituent atoms. Calculating larger systems results in computational times that were neither practical nor feasible. Other models sprang to give us density functional theory (DFT) as a method of using electron densities and energy functionals to significantly reduce the computational workload while still offering accurate results in a feasible timeframe.

##### 4.2.4.1 Electron density

Previous methods of finding solutions to the Schrödinger equation for an n-electron system were 3n-dimensional equations. A system built of solely 30 electrons would be a 90-dimension problem. We can see how by just increasing the number of atoms into double and triple digits the Schrödinger equation can become quite unreasonable to work with. However, the system can be massively simplified if we consider an electron density to describe n-electron systems. Strictly speaking, the electron density is a probability density and can be written as the sum of a set of squared occupied orbitals  $\phi_i$  (the wavefunction can be replaced by noninteracting orbitals, known as KS orbitals):

$$\rho(\vec{r}) = 2 \sum_i^{occ} |\phi_i(\vec{r})|^2 \quad (3)$$

$\rho(\vec{r})$  is the probability density of finding an electron in a given volume at point  $r$ . Naturally, the electron probability density integrates over space to give the total number of electrons in a system.

$$\int \rho(\vec{r}) d\vec{r} = n \quad (4)$$

Electron densities also have the added benefit of being observable quantities (they can be measured in a lab) whose value does not depend on the number of electrons in a system. Instead of a  $3n$ -dimension problem, it is reduced to a 3-dimensional density of electrons. Treating electron densities in place of wavefunctions would be key to developing DFT.

#### 4.2.4.2 Hohenberg-Kohn theorems

DFT is built upon two foundational theorems, the Hohenberg-Kohn (HK) theorems and state:

1. There is an external potential  $V_{ext}$  in the Hamiltonian that can be determined by the ground-state electron density.
2. The ground-state energy of a system can be determined using the variational principle.

The first theorem is based on facts regarding the electron density and the external potential. The external potential measures the interactions between the electron density and the nuclei in the fixed nuclei field. The nuclear attraction force is external to the electron density and is therefore regarded as an external potential, it is dependent on the system that is studied. The internal potential of the Hamiltonian is independent of the system, it involves the electronic kinetic energy term and the potential formed by electron-electron interactions. Because this potential is independent of the external potential, it is universal and can be applied to any system. Therefore, it is only necessary to know the ground-state electron density to define a system's external potential. If the internal potential of a Hamiltonian is the same for any given system, different Hamiltonians will differ solely on their external potential. In conclusion, the electron density of a system contains the necessary information to define its external potential, Hamiltonian, wave function, and all the ground-state properties of the system. The ground-state energy of a system is a unique functional of its electron density, hence *density functional theory*.

To start looking at the second theorem, let's first pay mind to an electron density  $\rho(\vec{r})$  that integrates into an  $n$ -number of electrons. According to the first theorem, the electron density will define the Hamiltonian acting on a candidate wave function  $\Psi$  to obtain an energy value  $E[\rho(\vec{r})]$ .

$$\int \Psi^* \hat{H} \Psi d\vec{r} = E[\rho(\vec{r})] \geq E_0 \quad (5)$$

Although this might be misleading in giving the idea of working with wave functions, in reality, HK DFT works with electron densities. So it may be better represented as:

$$E[\rho(\vec{r})] = E_{int}[\rho(\vec{r})] + E_{ext}[\rho(\vec{r})] \geq E_0 \quad (6)$$

where the density-dependant internal energy  $E_{int}[\rho(\vec{r})]$  is not explicitly known but its mathematical formula is the same for all systems as it's defined by system-independent internal potentials, and the external energy  $E_{ext}[\rho(\vec{r})]$  that is system dependant.

By evaluating the energy expectation value, an energy value  $E[\rho(\vec{r})]$  is found at electron density  $\rho(\vec{r})$  that is greater than or equal to ground state energy  $E_0$  of the system. At a given external potential  $V_{ext}$ , we can vary the electron density  $\rho(\vec{r})$  of the system to minimize the system energy until we reach the ground-state energy (but never below it). This is called the variational principle as it is applied to DFT.

#### 4.2.5 The Kohn-Sham approach to DFT

The early attempts to substitute the use of wave functions in favor of electron densities (which determine the external potentials and, thus the Hamiltonian of the Schrödinger equation) were not successful. The problem lay in the electron-electron interactions of the true Hamiltonian which made the solutions for the Schrödinger equation prohibitively difficult. In a moment of mathematical and abstract creativity only physicist display, in 1965 Kohn and Sham devised a method to consider the ground state density using a fictitious system of non-interacting electrons. Then, the Hamiltonian could be simplified to a sum of one-electron operators. In such a Hamiltonian, it would have eigenfunctions that are Slater determinants of the individual one-electron eigenfunctions, and where its eigenvalues would be the sum of the individual one-electron eigenvalues. The electron density holds the same position and atomic numbers of the nuclei, so this method for finding the energy eigenvalues would prove to be a lot more simple and approachable.

Let us write the eigenvalue known as the energy for interacting electrons using the HF method. This energy would include terms relating to the kinetic ( $E_{kin}$ ) and external ( $E_{ext}$ ) energies. We also have two energy terms as a result of the HF, the Hartree energy ( $E_H$ ) and exchange energies ( $E_x$ ), so that (we will be excluding the density function for simplicity):

$$E = E_{kin} + E_{ext} + E_H + E_x \quad (7)$$

Using the KS approach to consider n-electron energies into n one-electron energies at ground state:

$$E_{kin} = E_{kin}^{non} + E_{kin}^{int} \quad (8)$$

and

$$E_H + E_x = E_x + E_x + E_c^{int} \quad (9)$$

where noninteracting and interacting kinetic energies are denoted by the *int* superscript. These are also called the correlating energies, and a new "correlation" energy term is introduced. Grouping the correlation and exchange energies into an "exchange-correlation energy", we arrive at:

$$E_{xc} = E_x + E_x^{int} + E_{kin}^{int} = E_x + E_c \quad (10)$$

This gives the final expression of the total energy in the framework of DFT.

$$E = E_{kin}^{non} + E_{ext} + E_H + E_{xc} = E_{int}[\rho(\vec{r})] + E_{ext}[\rho(\vec{r})] \quad (11)$$

While the internal energy terms are easy to calculate, the  $E_{xc}$  is unknown and therefore approximated. Finally, the nuclei-nuclei interactions are added as a constant derived from the Born-Oppenheimer approximation.

Applying the KS approach to the Hamiltonian:

$$\hat{H}_{KS} = E_{kin}^{non} + V_{ext} + V_H + V_{xc} = -\frac{1}{2}\nabla^2 + V_{eff} \quad (12)$$

where the effective potential  $V_{eff}$  is that of the ground-state electron density of the noninteracting electron system and determines it to be identical to the real electron-electron interacting system.

## 4.2.6 Exchange-correlation functional

The exchange-correlation density functional  $E_{\rho(\vec{r})}$ , as derived from the Kohn-Sham method, includes the difference between the fictitious non-interacting system and the real system. This functional is unknown, so we have to approximate this quantity as much as possible to be able to accurately predict the total energy of a system, and thus, its properties. An exchange-correlation hole is introduced that calculates the kinetic energy difference between the non-interacting and interacting systems. The functional is expressed as:

$$E_{xc}[\rho(\vec{r})] = \int \rho(\vec{r})\epsilon_{xc}[\rho(\vec{r})]d\vec{r} \quad (13)$$

$\epsilon_{ex}$  is the energy density calculated as the sum of the exchange and correlation contributions.

### 4.2.6.1 Local density approximation

The local density approximation (LDA) exchange-correlation energy functional assumes the differentiation of a uniform electron density into many small or "local" pieces. The exchange-correlation energy density  $\epsilon_{xc}[\rho(\vec{r})]$  at a local position  $\vec{r}$  is then used calculate the XC energy functional  $E_{xc}$ :

$$E_{xc}^{LDA}[\rho(\vec{r})] = \int \rho(\vec{r})\epsilon_{xc}^{hom}[\rho(\vec{r})]d\vec{r} \quad (14)$$

where  $\epsilon_{xc}^{hom}[\rho(\vec{r})]$  is the local energy density of a homogeneous electron gas.

### 4.2.6.2 Generalized gradient approximation

The generalized gradient approximation considers both the electron density  $\rho(\vec{r})$  and the density gradient  $\nabla\rho(\vec{r})$  at a given point. This considers the fact that real systems are not as homogeneous as an electron gas might be and therefore should give more accurate XC energy functionals and results. Its general form is:

$$E_{xc}^{GGA}[\rho(\vec{r})] = \int \rho(\vec{r})\epsilon_{xc}^{GGA}[\rho(\vec{r}), \nabla\rho(\vec{r})]d\vec{r} \quad (15)$$

This thesis uses a revised version of the GGA approximation as parametrized by PBE (*CITE*) that has proved to be computationally efficient while offering accurate results, as its implemented in VASP.

### 4.2.7 Pseudopotentials

Pseudopotentials (PP) make use of a frozen nucleus and core electrons in a system to streamline the computation for large solid structures, effectively creating, or "pseudizing", the valence electron wave functions for easier calculations. The core electrons in a solid molecular system are (mostly) unchanging under external forces, sticking tightly to the nucleus of their respective atoms. They are at the bottom of a deep potential well. The valence electrons find themselves at the top of this potential well, quickly reacting with their environment. They are responsible for forming chemical bonds and may even travel through the sea of electrons in a metal. The valence wave functions also react with the core states in an all-electron (AE) system. When calculating the Hartree potential energy from the wave function, there are big nodes that are computationally demanding to solve. If the core is considered frozen, the valence electrons become the lowest states available, smoothing out the wave functions nodes and their corresponding potentials, as seen in figure 3.

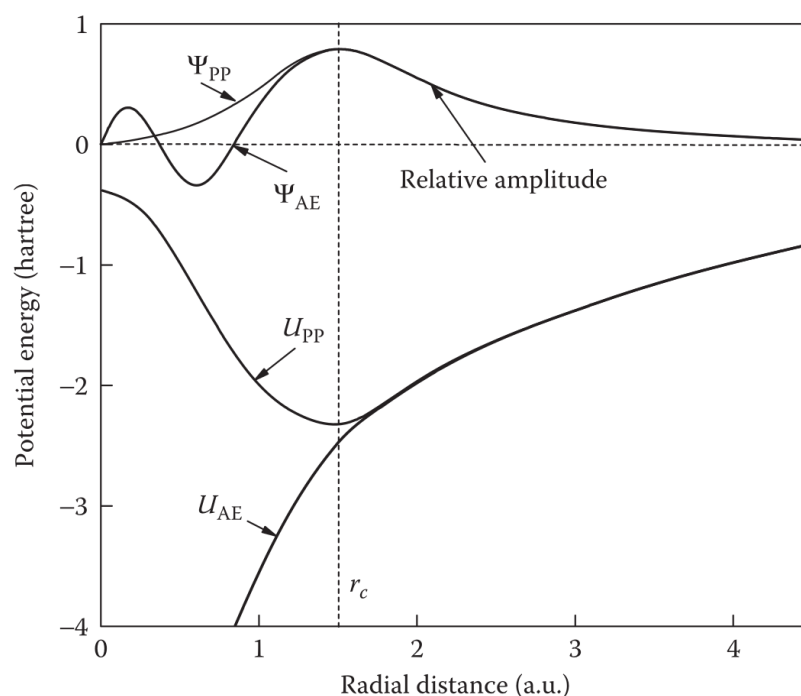


Figure 3. Illustration showcasing the "smoothing" of the wave function and its corresponding potential, also called the pseudopotential, in comparison to an all-electron (AE) wave function. Graph borrowed from June Gunn Lee's book "Computational Materials Science: An Introduction" (2016).

This thesis makes use of the projector-augmented wave (PAW) pseudopotential. This PP method considers both the valence wave function  $\Psi_{val}$  and core wave function  $\Psi_{core}$ , projecting the former over the latter. The resulting wave function  $\Psi_{net}$  of their overlap is removed to make a wave function  $\Psi_{PAW}$  that gives more accurate results closer to the true AE wave function with less computational

effort:

$$\Psi_{PAW} = \Psi_{val} + \Psi_{core} - \Psi_{net} \quad (16)$$

#### 4.2.8 Surface Formation Energy Formalism

The  $Ti_2Ta_2C_3Tz$  MXene systems we are working with vary in both size and surface chemistry (due to the different chemical species involved). Thus, we make use of a surface formation energy formalism to investigate the thermodynamic stability of our MXenes. This formalism depends on the chemical potentials of the species involved rather than its number of atoms. We apply the concepts of free energy and chemical potential  $\mu_i$  of each  $i$  atom to study the system's stability.

Gibb's free energy is a measure of the work done in a system at constant pressure and temperature. If the change in Gibb's free energy is negative ( $\Delta G < 0$ ), it's an indication of a thermodynamically favorable reaction of a physical or chemical process. Eventually, this value will reach a minimum energy level that defines the system's thermodynamic equilibrium and where no further change will occur. The chemical potential  $\mu_i$  is the derivative of Gibb's free energy with respect to the number of  $i$  atoms (Qian et al., 1988):

$$\mu_i = \frac{dG}{dn_i} = \frac{d(E + PV - TS)}{dn_i} \quad (17)$$

where  $E$  is the total energy,  $P$  is pressure,  $V$  is volume,  $T$  is temperature,  $S$  is entropy, and  $n_i$  is the number of atoms of the  $i$ th species. Because we work with condensed crystalline phases and we do not consider temperature, the chemical potentials can be simplified to:

$$\mu_i = \frac{E}{n_i} \quad (18)$$

The surface formation energy can be written as

$$E_f = E_T - E_R - \sum n_i \mu_i \quad (19)$$

where  $E_T$  is the total energy of the studied system (functionalized MXene in our case) and  $E_R$  is a reference energy (pristine MXene). However, the lattice parameter of our structures vary in their most

stable state and, thus, their surface areas varies as well. We need to normalize our surface formation energy by surface area to obtain comparable results. The area-normalized surface formation energy used throughout this thesis is:

$$E_F = \frac{1}{A}(E_T - E_R - \sum n_i \mu_i) \quad (20)$$

where  $A$  is the surface area of the system of interest.

#### 4.2.9 Open Circuit Voltage

The formation energy is also used to study the electrochemical properties of the MXene structures in the form of its open circuit voltage (OCV). The OCV is related to the surface formation energy as follows (Er et al., 2014):

$$OCV = -\frac{E_f}{n_{Li}} \quad (21)$$

where  $n_{Li}$  is the number of lithium adatoms on the cell surface.

## Chapter 5. Results & Discussion

### 5.1 MAX-phase

To start, a MAX-phase crystal structure acquired from The Materials Project served as the precursor material for building the  $\text{Ti}_2\text{Ta}_2\text{C}_3$  unit cell. We began working with a Crystallographic Information File (.cif) that contained the information of a  $\text{Ti}_4\text{AlN}_3$  MAX-phase hexagonal crystal structure with two formula units per unit cell, as can be appreciated in figure 4. The file (.cif) contains optimized information on the chosen crystallographic structure, such as cell geometry (lengths & angles), cell volume, crystal lattice system, and atomic positions. The MAX-phase nitride material had the  $a = b = 2.98 \text{ \AA}$  and  $c = 23.42 \text{ \AA}$  lattice parameters and a cell volume of  $180.65 \text{ \AA}^3$ . VESTA was used to read and manipulate the data from the .cif file containing the MAX-phase material. The desired material forms a carbide structure; therefore, all nitrogen positions were exchanged for carbon atoms to obtain a MAX-phase  $\text{Ti}_4\text{AlC}_3$ .

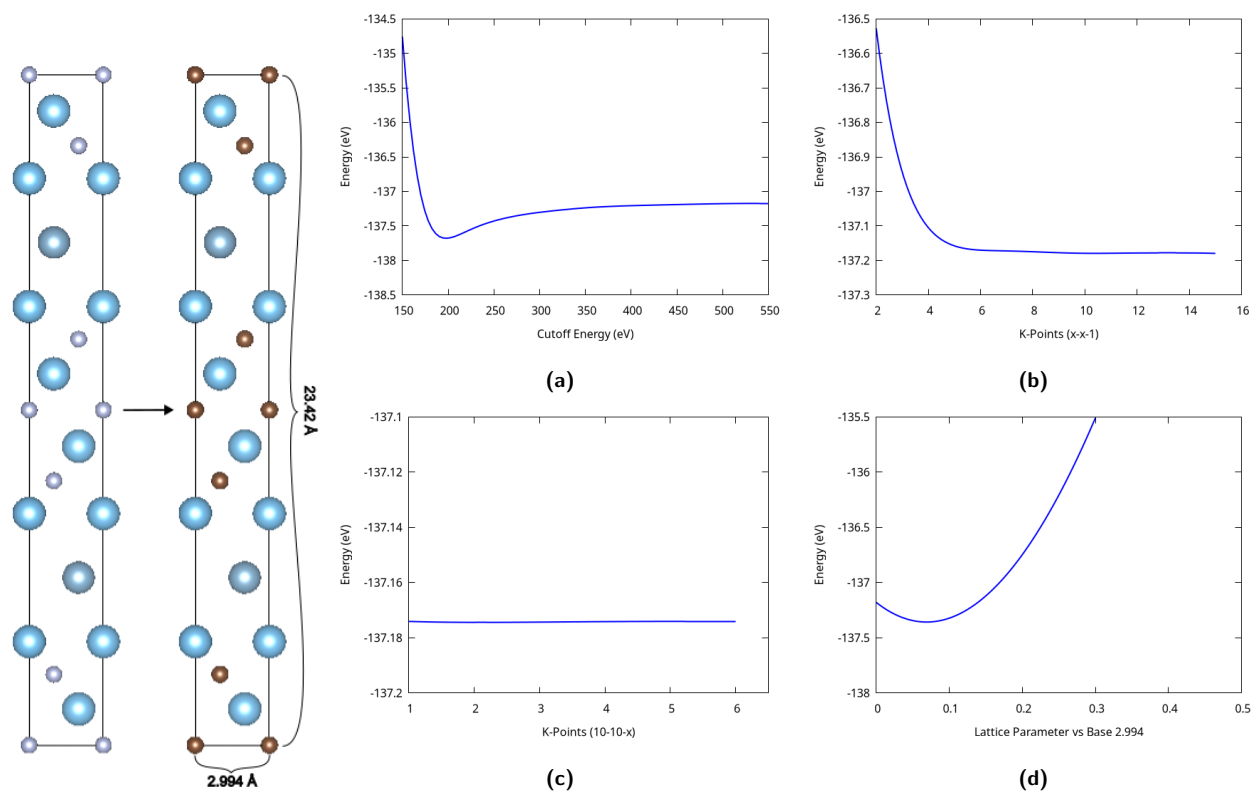


Figure 4.  $\text{Ti}_4\text{AlN}_3$  to  $\text{Ti}_4\text{AlC}_3$ . Figure 5. Optimization plots for  $\text{Ti}_4\text{AlC}_3$ : a) cutoff energy, b) k-points (x-x-1), c) k-points (10-10-x), and d) lattice parameter.

### 5.1.1 Optimization

Although the titanium nitride structure provided by The Materials Project was structurally optimized beforehand, modifying the chemical structure of the crystalline unit cell meant that the previously calculated information was no longer valid. Therefore, we optimized our newly created MAX-phase titanium carbide structure.

First, we varied the cutoff energy for the plane wave basis until we reached convergence. We considered an energy difference of 0.01 eV for our convergence criteria. Figure 5a shows that an acceptable cutoff energy convergence at 340 eV was reached. However, final self-consistent field calculations considered a cutoff energy 1.3x greater than the maximum cutoff energy specified in the POTCAR files of constituent species found in the MAX carbide structure, as is the convention for results that balances calculation accuracy vs. calculation time. The POTCAR files contain the atomic species' pseudopotentials.

Secondly, we optimized the k-points, or the Bloch vectors, used to sample the Brillouin zone. VASP offers various methods of specifying the k-points in the input files, we used a Monkhorst-Pack k-point mesh automatically generated by VASP by defining its number of subdivisions. The reason for this is that it offers sufficient flexibility and stability for most calculation purposes while maintaining simple k-point mesh criteria. It depends on three variables representative of the number of subdivisions of the reciprocal lattice vectors and is described as  $a_1$ - $a_2$ - $a_3$ . We set the variable concerning the vector in the  $a_3$  direction as 1 as we varied the Monkhorst-Pack scheme mesh in both  $a_1$  and  $a_2$  directions until convergence. Figure 5b shows acceptable convergence at values starting at 5-5-1, with greater stabilization starting at 10-10-1. Therefore, as increasing the k-point mesh vastly increases compute time, we find a good balance of accuracy vs. time at 10-10-1. Now that the mesh was optimized at  $a_1$  and  $a_2$ ,  $a_3$  could now be optimized at constant  $a_1$  and  $a_2$ . Figure 5c shows a high level of convergence stability starting at 10-10-1. These results served as a basis for all subsequent calculations; as these parameters could be transferred for the optimization of the MXene structure, a large amount of compute time and power was saved having only the need to optimize the crystal lattice moving forward.

Finally, the lattice parameter was optimized until its point of minimum energy, as shown in Fig. 5d.  $\text{Ti}_4\text{AlC}_3$  is a hexagonal crystal structure, so its lattice parameters  $a$  and  $b$  are equal. We reached a point of minimum energy at a lattice parameter of  $a = 3.094 \text{ \AA}$ . This result shows conformity with previously reported experimental results; Eklund et. al. (2007) measured, using synchrotron X-ray diffraction data, a lattice parameter of  $a = 3.109 \text{ \AA}$  in a synthesized  $\text{Ti}_4\text{AlC}_3$  structure.

## 5.2 MXene

### 5.2.1 $\text{Ti}_4\text{C}_3$

Building a  $\text{Ti}_4\text{C}_3$  MXene is as straightforward as removing the Al atoms from the  $\text{Ti}_4\text{AlC}_3$  unit cell, as is shown in Figure 6. In addition to removing the Al, we removed atoms from the upper and lower extremes of our unit cell to reduce it to one formula unit per cell. However, we did not reduce the cell size in the c-direction to fit our newly created unit cell. Instead, we created a vacuum of around 14 Å to avoid self-interactions that may occur due to periodic boundary conditions.

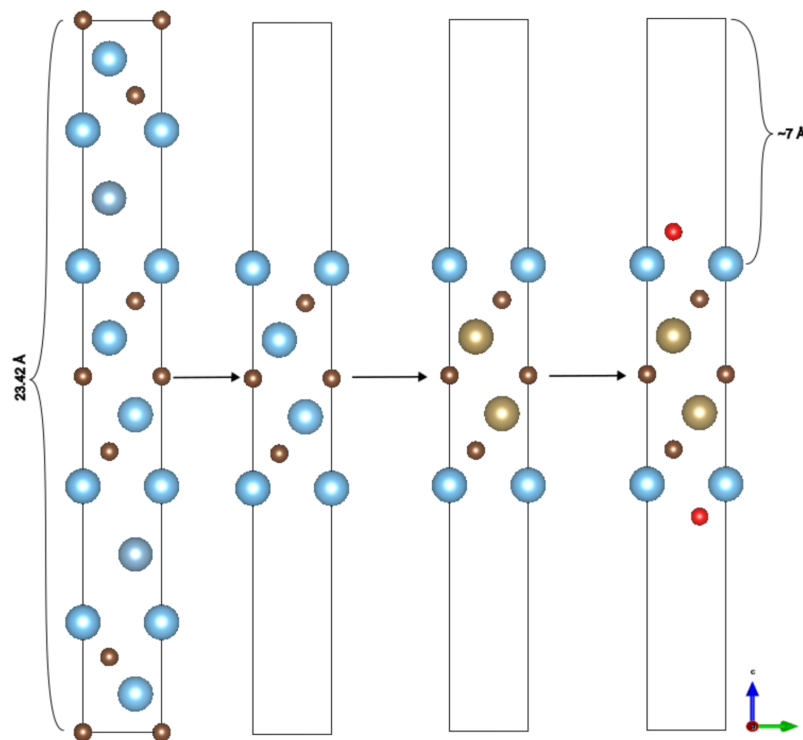


Figure 6. Schema showing how the  $\text{Ti}_2\text{Ta}_2\text{C}_3\text{T}_z$  MXene was built from a MAX-phase  $\text{Ti}_4\text{AlC}_3$  starting point. Ti, Al, Ta, and C are represented by the blue, red, yellow, and brown spheres, respectively.

A 10-10-1 Monkhorst-Pack k-point mesh offered excellent convergence values for  $\text{Ti}_4\text{C}_3$ . The optimized structure presented a lattice parameter  $a = 3.094$  (fig. 7). This value comes fairly close to other reported DFT studies using similar methods (GGA-PBE functional); García-Romeral et al. (2023) predicted a lattice parameter  $a = 3.10$  Å for non-magnetic  $\text{Ti}_4\text{C}_3$ , while other notable works by Shein (2012) and Kurtoglu (2012) predicted lattice parameters  $a = 3.09$  Å and  $a = 3.07$  Å, respectively. Therefore, our results are in good agreement with previously reported studies on  $\text{Ti}_4\text{C}_3$ .

### 5.2.2 $\text{Ti}_2\text{Ta}_2\text{C}_3$

Maldonado's et al., research (2021) demonstrated the highest level of thermodynamic stability for  $\text{Ti}_2\text{Ta}_2\text{C}_3$  when the Ta atoms fill the inner layers of the atomic hepta-layer  $\text{Ti}_2\text{Ta}_2\text{C}_3$  MXene. Therefore, we substituted the inner Ti layers of our  $\text{Ti}_4\text{C}_3$  with Ta atoms to build the ordered alloy  $\text{Ti}_2\text{Ta}_2\text{C}_3$  MXene. The resulting structure can be appreciated in Fig. 6. Fig. 8 shows the optimization process for its lattice parameter, showing stable results at  $a = 3.094$ .

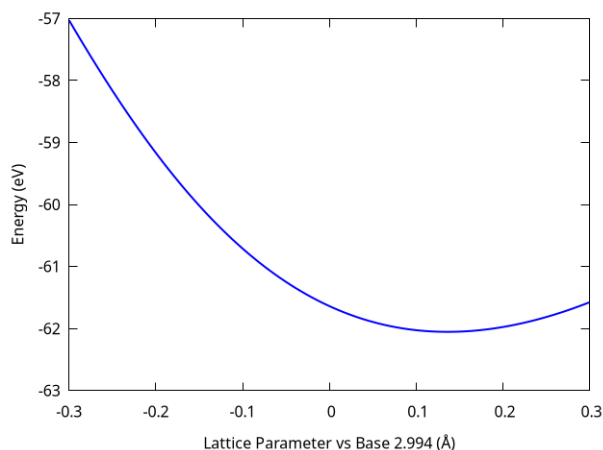


Figure 7.  $\text{Ti}_4\text{C}_3$  lattice parameter optimization.

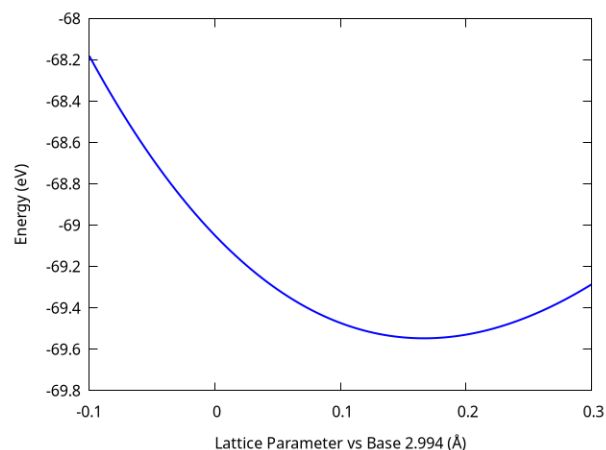


Figure 8.  $\text{Ti}_2\text{Ta}_2\text{C}_3$  lattice parameter optimization.

### 5.2.3 $\text{Ti}_2\text{Ta}_2\text{C}_3\text{T}_z$

A functionalization process was used to systematically introduce O-, F-, Cl-, and OH- functional groups onto our cell surface. Figure 6 shows how this process was done schematically. The functional groups were introduced in four high-symmetry sites on the surface of our crystalline material, as shown in figure 9. These are described as follows:

- **Bridge:** The functional group is placed at the middle point between the two most exposed atoms (Ti) on the pristine MXene surface.
- **Hollow or H3:** Directly above the third atomic layer below (Ta).
- **T4:** Directly above the second atomic layer below (C).
- **Top:** Directly above the first atomic layer below (Ti).

The introduction of the functional group may modify the lattice parameter of the MXene unit cell. Table 1 shows a comparison between the lattice parameters of the optimized structures for all four

functional groups in addition to a reference pristine  $\text{Ti}_2\text{Ta}_2\text{C}_3$ . In general, we can see that the Bridge and Top sites, in addition to the larger Cl functional group in  $\text{Ti}_2\text{Ta}_2\text{C}_3\text{Cl}_2$ , increase the lattice parameter by 0.1 Å. The H3 and T4 sites for O, F, and OH functional groups maintained a lattice parameter  $a = 3.094$  Å with a couple of exceptions. A larger lattice parameter may indicate lower Li storage volumetrically in  $\text{Ti}_2\text{Ta}_2\text{C}_3\text{T}_z$  as Li-ion battery anode material.

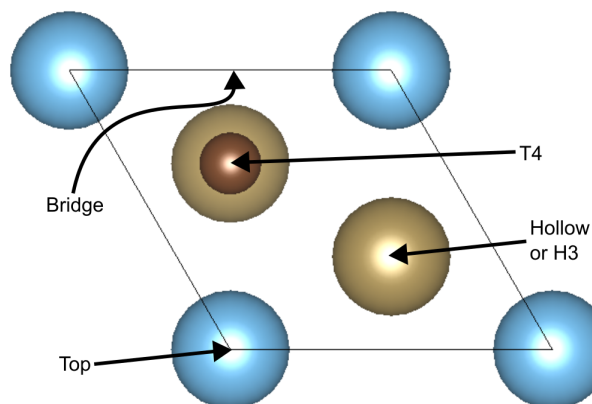


Figure 9. Top view of a  $\text{Ti}_2\text{Ta}_2\text{C}_3$  unit cell showing the positions of the four high-symmetry sites.

Table 1. Functionalized MXene lattice parameter in Å compared to pristine  $\text{Ti}_2\text{Ta}_2\text{C}_3$ . In pristine form, no functional group is considered.

System	Br	H3	T4	Top
Pristine		3.094		
$\text{Ti}_2\text{Ta}_2\text{C}_3\text{O}_2$	3.194	3.094	3.094	3.194
$\text{Ti}_2\text{Ta}_2\text{C}_3\text{F}_2$	3.094	3.094	3.094	3.194
$\text{Ti}_2\text{Ta}_2\text{C}_3\text{Cl}_2$	3.194	3.194	3.194	3.194
$\text{Ti}_2\text{Ta}_2\text{C}_3(\text{OH})_2$	3.094	3.094	3.094	3.194

### 5.3 2x2 Supercell

Until now, we have been working with a single formula unit cell. That is to say, our unit cell represented a single chemical formula unit of  $\text{Ti}_2\text{Ta}_2\text{C}_3$ . To be able to introduce different concentrations of Li per formula unit cell we increased the volume of our unit cell by increasing its surface area to obtain a 2x2  $\text{Ti}_2\text{Ta}_2\text{C}_3$  supercell as seen in figure 10. Although this significantly increased the computing power required and thus the time to carry out the computations, due to the number of atoms per unit cell increasing by a factor of 4, we would not be able to study the effects of partial lithium content per

formula unit cell otherwise. Fortunately, the computing power proved to be sufficient to perform the calculations on time.

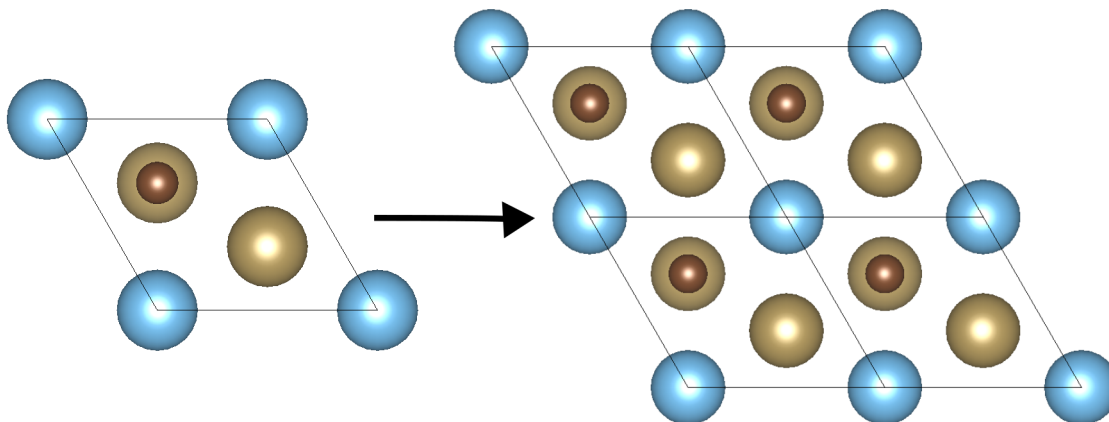


Figure 10. Transformation of a  $\text{Ti}_2\text{Ta}_2\text{C}_3$  formula unit cell into a  $2 \times 2$   $\text{Ti}_2\text{Ta}_2\text{C}_3$  supercell.

### 5.3.1 Crystal lattice optimization

With the cutoff energy set to a constant 520 eV and a Monkhorst-Pack k-point mesh with values 5-5-1 (the increase in cell size causes a proportional modification of the k-point mesh due to a smaller Brillouin zone), the next step of optimization for the supercell MXenes is to optimize its crystal lattice to a minimum energy point. We varied the volume, by varying surface area solely, of the crystal cell until a point of minimum energy was observed. This proved to be a challenge for both compute power and time as the number of cells needed to be geometrically optimized was substantially large; even before the lithiation process, each cell for each functional group for each high-symmetry site was geometrically optimized until a parabolic curve was observed and a point of minimum energy was found.

Table 2. Functionalized  $2 \times 2$  supercell MXene lattice parameter in Å.

System	Br	H3	T4	Top
$\text{Ti}_2\text{Ta}_2\text{C}_3\text{O}_2$	6.29	6.19	6.19	6.49
$\text{Ti}_2\text{Ta}_2\text{C}_3\text{F}_2$	6.19	6.19	6.19	6.39
$\text{Ti}_2\text{Ta}_2\text{C}_3\text{Cl}_2$	6.39	6.39	6.29	6.39
$\text{Ti}_2\text{Ta}_2\text{C}_3(\text{OH})_2$	6.29	6.29	6.19	6.39

As expected, the most stable functionalized MXene cell varied according to the size and position of its functional group. Larger, heavier atoms caused the cell to expand in size, as well as high-symmetry

sites that were not energetically favorable. Table 2 summarizes the cell size for each functional group at each high-symmetry site for its most stable configuration. The disparity in cell size found in other high-symmetry sites can be attributed to rounding errors; a lattice parameter variation of 0.1 Å was used for the optimization, a finer variation will marginally improve the results but greatly increase the compute power and time required.

Table 3. Functionalized 2x2 supercell MXene relative energies in eV.

<b>System</b>	<b>Br</b>	<b>H3</b>	<b>T4</b>	<b>Top</b>
Ti <sub>2</sub> Ta <sub>2</sub> C <sub>3</sub> O <sub>2</sub>	0.48	<b>0.00</b>	6.03	17.65
Ti <sub>2</sub> Ta <sub>2</sub> C <sub>3</sub> F <sub>2</sub>	10.04	<b>0.00</b>	2.12	6.36
Ti <sub>2</sub> Ta <sub>2</sub> C <sub>3</sub> Cl <sub>2</sub>	3.61	<b>0.00</b>	0.86	7.98
Ti <sub>2</sub> Ta <sub>2</sub> C <sub>3</sub> (OH) <sub>2</sub>	<b>0.00</b>	<b>0.00</b>	0.95	6.09

To find the most stable high-symmetry site for each functional group, relative energies were calculated with the most stable site (the site with the least amount of energy) as the baseline is shown in table 3. All functionalized MXene groups were most stable in the H3 site configuration. OH appears to be similarly stable at site Bridge but upon further inspection of this peculiar phenomenon, we found that the OH functional group moved and stabilized at H3. As expected due to larger lattice parameters, the Top site was generally the most unstable. T4, with slightly narrower spacing than the H3 site, proved to be the second most favorable site for the functional groups. This is important as lithiation (the insertion of lithium atoms to the cell surface) was done in the most stable site initially, but if the MXene demonstrated thermodynamic stability at full surface coverage, lithium adatoms were also introduced in the second-most stable site. We discuss the lithiation process in more detail in section 5.4.1.

### 5.3.2 Thermodynamic stability of Ti<sub>2</sub>Ta<sub>2</sub>C<sub>3</sub>T<sub>z</sub> MXenes

To observe the chemical stability of the functional groups on the surface of the MXene material, we calculated the formation energy for the most stable site for each functional group. However, due to the different chemical compositions and surface area of the functionalized MXene materials, we employed the area-normalized surface formation energy (SFE) formalism. The most stable systems exhibit lower energy values. All products proved to be thermodynamically stable, as can be appreciated in table 4.

Table 4. Surface formation energy results for the most stable high-symmetry site of each group.

System (H3)	SFE (eV/Å <sup>2</sup> )
Ti <sub>2</sub> Ta <sub>2</sub> C <sub>3</sub> O <sub>2</sub>	-1.73
Ti <sub>2</sub> Ta <sub>2</sub> C <sub>3</sub> F <sub>2</sub>	-1.88
Ti <sub>2</sub> Ta <sub>2</sub> C <sub>3</sub> Cl <sub>2</sub>	-1.09
Ti <sub>2</sub> Ta <sub>2</sub> C <sub>3</sub> (OH) <sub>2</sub>	-1.31

### 5.3.3 Electronic Properties

#### 5.3.3.1 Band structure

Here we present a band structure analysis to verify the potential performance of the functionalized Ti<sub>2</sub>Ta<sub>2</sub>C<sub>3</sub> MXenes as anode material. One of the advantages of the tunable band gap properties of MXenes is derived from their functional groups, however, an electrode in a Li-ion battery is required to be an electrical conductor. If a band gap is present, electrical conductivity is reduced greatly impacting the performance of the Li-ion battery. It is advantageous to use metallic materials rather than semiconductors as electrode material in Li-ion batteries.

A band structure analysis was performed using the  $\Gamma - M - K - \Gamma$  high-symmetry path along the hexagonal Brillouin zone. Figure 11 displays the band structures for the pristine Ti<sub>2</sub>Ta<sub>2</sub>C<sub>3</sub> and select Ti<sub>2</sub>Ta<sub>2</sub>C<sub>3</sub>T<sub>z</sub> for one high-symmetry site each. We found overlapping of the valence bands above the Fermi energy level for pristine and all functionalized Ti<sub>2</sub>Ta<sub>2</sub>C<sub>3</sub> MXenes, suggesting a metallic nature for the ordered-alloy MXene in all of its chemical and structural compositions. Band degeneracy and highly dispersive bands can be observed suggesting high charge carrier mobility. This helps prove the viability of Ti<sub>2</sub>Ta<sub>2</sub>C<sub>3</sub>T<sub>z</sub> as electrode material for Li-ion batteries.

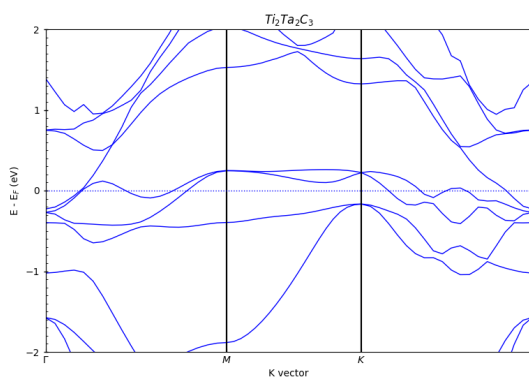
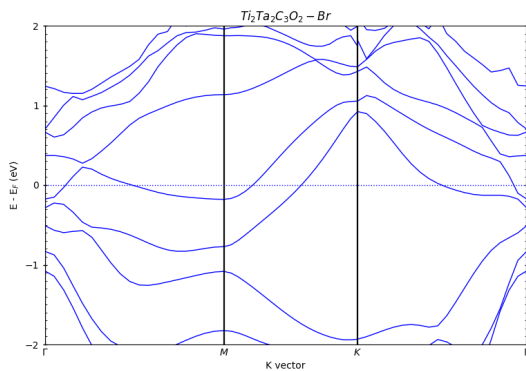
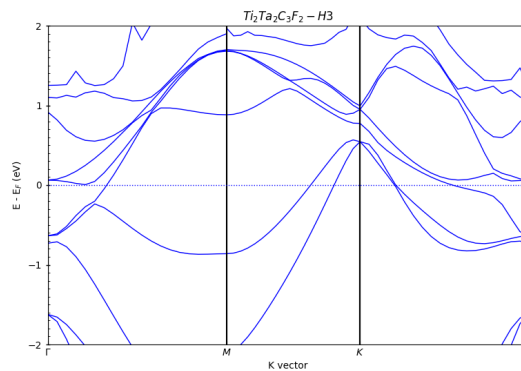
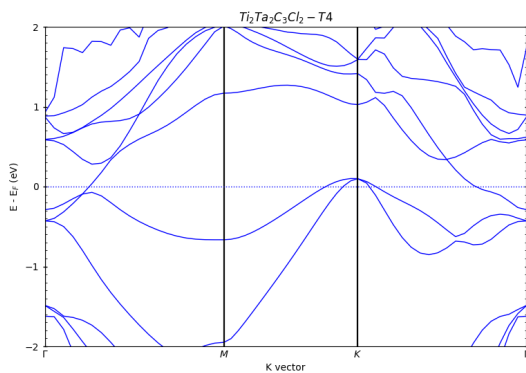
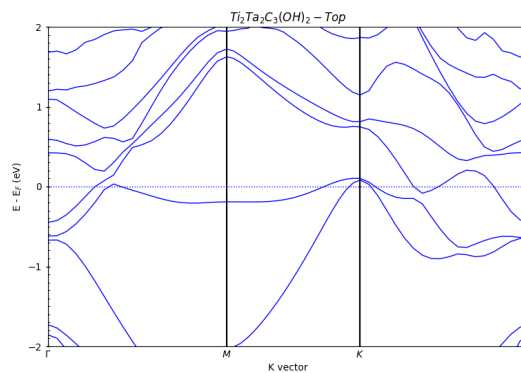
(a) Band structure plot for pristine  $\text{Ti}_2\text{Ta}_2\text{C}_3$ (b) Band structure plot for  $\text{Ti}_2\text{Ta}_2\text{C}_3\text{O}_2\text{-Br}$ (c) Band structure plot for  $\text{Ti}_2\text{Ta}_2\text{C}_3\text{F}_2\text{-H3}$ (d) Band structure plot for  $\text{Ti}_2\text{Ta}_2\text{C}_3\text{Cl}_2\text{-T4}$ (e) Band structure plot for  $\text{Ti}_2\text{Ta}_2\text{C}_3(\text{OH})_2\text{-Top}$ 

Figure 11. Band structures for 11a)  $\text{Ti}_2\text{Ta}_2\text{C}_3$ , 11b)  $\text{Ti}_2\text{Ta}_2\text{C}_3\text{O}_2\text{-Br}$ , 11c)  $\text{Ti}_2\text{Ta}_2\text{C}_3\text{F}_2\text{-H3}$ , 11d)  $\text{Ti}_2\text{Ta}_2\text{C}_3\text{Cl}_2\text{-T4}$ , and 11e)  $\text{Ti}_2\text{Ta}_2\text{C}_3(\text{OH})_2\text{-Top}$ .

### 5.3.3.2 Electrostatic potential isosurfaces

We calculated the electrostatic potential isosurfaces (EPI) to gain insights on the electrostatic potential distribution on the surfaces of the functionalized MXenes as we shown in figure 12. All EPIs are in the RGB scheme, where blue color denotes a positive electrostatic potential, red is for a negative electrostatic potential, and green suggests a neutral potential. Figures 12a, 12b and 12c correspond to the O-, F-, and Cl-functionalized MXenes, respectively. The surface provides a negative potential while the inner Ti (C) atoms remain positive (negative). This result suggests that the surface of the MXene is susceptible to electrophilic attacks from positively charged Li-ions. On the other hand, the OH-functionalized MXene (Fig. 12d) shows positive regions over the surface that comes from the H atoms of the OH functional group, these zones can work as the repulsive centers for the Li intercalation process.

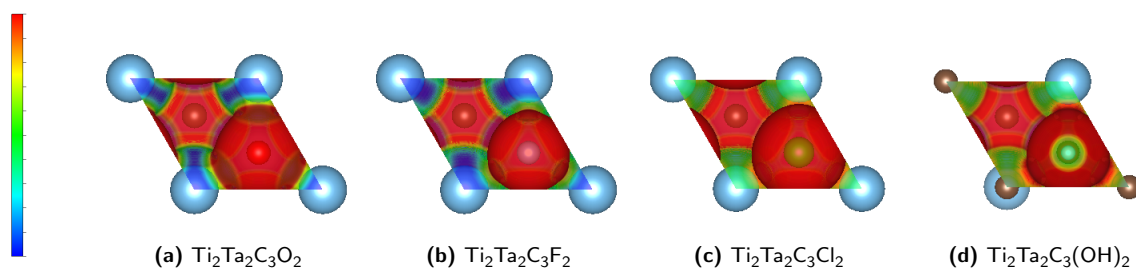


Figure 12. Electrostatic potential isosurfaces for O-, F-, Cl-, and OH-functionalized  $\text{Ti}_2\text{Ta}_2\text{C}_3$  MXenes in the H3 high-symmetry site in top view.

## 5.4 Lithiated MXenes

### 5.4.1 Description of the lithiation process on the cell surface

From Maldonado's (2021) study, we know that the lithiation process favors lithium adatom incorporation onto the surface of the chemically ordered MXene. From this premise, we systematically introduced lithium adatoms onto the surface of our functionalized MXene structures. We used the same four high-symmetry sites as for the functional groups, but this time the functional group serves as the base for site location. That is to say, the direct monoatomic layer below the incorporated lithium-ion was not the surface of the pristine MXene material but rather the functional group layer. The four high-symmetry sites used were Bridge, H3, T4, and Top. As the H3 site was the most stable configuration for all functional groups, the lithiation process was performed and lithium was incorporated on top of the H3 site for all functional groups. To avoid confusion, it must be clarified that lithium was incorporated on-site according to the H3 site corresponding to the functional group, but lithium was introduced into

the four high-symmetry sites corresponding to the position of the lithium ion. A more visual approach to this process can be appreciated in figure 13.

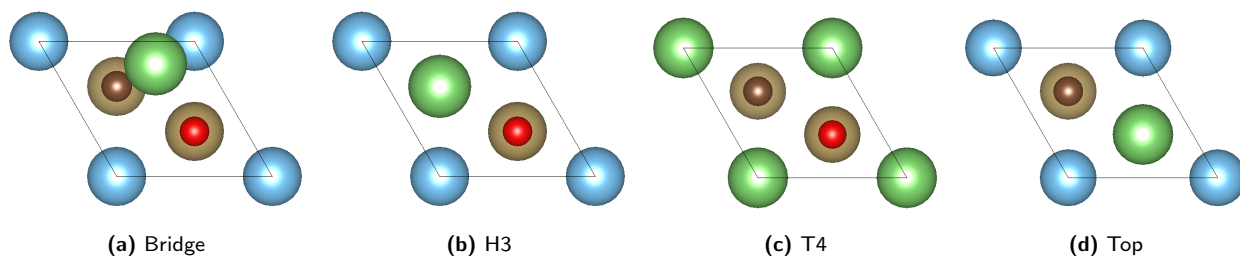


Figure 13.  $\text{Ti}_2\text{Ta}_2\text{C}_3\text{Li}$  unit cell top view displaying the Li adatom in four high-symmetry sites: a) Bridge, b) H3, c) T4, and d) Top. All four variants use a base H3 high-symmetry site for the functional group.

For each high-symmetry site, we introduced lithium ions until full lithium concentration on the cell surface, or until the system was no longer chemically stable as lithium concentration increased per unit cell. Table 5 shows the relative energies corresponding to 0.25, 0.5, 0.75, and 1 lithium atoms per formula unit cell. Figure 13 shows how this was done using a base  $\text{Ti}_2\text{Ta}_2\text{C}_3\text{O}_2$  H3 (functional group) supercell in the ion site H3 until the surface of the cell reached full lithiation. From table 5, we observe that lithium ions generally preferred the H3 site, similar to the functional group high-symmetry site, displaying the lowest relative energy values for MXenes functionalized with O, F, and OH. This trend continued through the saturation of the cell surface with lithium ions. However, the Cl-functionalized MXenes behaved differently; lithium ions preferred the T4 site for the chlorinated MXene. There is also a discontinuity in the results for OH-functionalized MXenes beyond a lithium concentration of 0.25 per formula unit cell, this is explained in the next subsection.

Table 5. Relative energies (eV) for the lithiated MXene at various lithium concentrations per formula unit cell.

System	Br	H3	T4	Top	System	Br	H3	T4	Top
$\text{Ti}_2\text{Ta}_2\text{C}_3\text{O}_2\text{Li}_{0.25}$	0.75	<b>0.00</b>	0.53	0.81	$\text{Ti}_2\text{Ta}_2\text{C}_3\text{O}_2\text{Li}_{0.5}$	1.03	<b>0.00</b>	0.80	2.16
$\text{Ti}_2\text{Ta}_2\text{C}_3\text{F}_2\text{Li}_{0.25}$	0.25	<b>0.00</b>	0.14	0.89	$\text{Ti}_2\text{Ta}_2\text{C}_3\text{F}_2\text{Li}_{0.5}$	0.54	<b>0.00</b>	0.26	1.09
$\text{Ti}_2\text{Ta}_2\text{C}_3\text{Cl}_2\text{Li}_{0.25}$	0.21	0.03	<b>0.00</b>	0.94	$\text{Ti}_2\text{Ta}_2\text{C}_3\text{Cl}_2\text{Li}_{0.5}$	0.34	0.60	<b>0.00</b>	1.02
$\text{Ti}_2\text{Ta}_2\text{C}_3(\text{OH})_2\text{Li}_{0.25}$	0.02	<b>0.00</b>	0.02	0.53	$\text{Ti}_2\text{Ta}_2\text{C}_3(\text{OH})_2\text{Li}_{0.5}$	-	-	-	-
$\text{Ti}_2\text{Ta}_2\text{C}_3\text{O}_2\text{Li}_{0.75}$	1.39	<b>0.00</b>	1.32	2.75	$\text{Ti}_2\text{Ta}_2\text{C}_3\text{O}_2\text{Li}$	1.55	<b>0.00</b>	1.50	2.86
$\text{Ti}_2\text{Ta}_2\text{C}_3\text{F}_2\text{Li}_{0.75}$	1.45	<b>0.00</b>	0.48	1.80	$\text{Ti}_2\text{Ta}_2\text{C}_3\text{F}_2\text{Li}$	1.82	<b>0.00</b>	0.23	1.96
$\text{Ti}_2\text{Ta}_2\text{C}_3\text{Cl}_2\text{Li}_{0.75}$	0.42	0.20	<b>0.00</b>	0.89	$\text{Ti}_2\text{Ta}_2\text{C}_3\text{Cl}_2\text{Li}$	0.16	0.18	<b>0.00</b>	0.39
$\text{Ti}_2\text{Ta}_2\text{C}_3(\text{OH})_2\text{Li}_{0.75}$	-	-	-	-	$\text{Ti}_2\text{Ta}_2\text{C}_3(\text{OH})_2\text{Li}$	-	-	-	-

### 5.4.2 Thermodynamic stability of the lithiated MXenes

Table 6 shows the thermodynamic stability of the lithiated MXene materials for each functional group in its most stable high-symmetry site. This was calculated using the area-normalized surface formation energy formalism that allows the comparison of different stoichiometric. These results show that the hydroxylated MXene is no longer thermodynamically stable after receiving the lithium ion, therefore we no longer considered it a viable option for Li-ion energy storage devices.

Moving on to the stable  $Ti_2Ta_2C_3T_zLi_x$  structures, we observe maximum lithium concentration points for Cl, F, and O functional groups at  $x=0.5, 1.25,$  and  $2,$  respectively. After reaching the highest lithium concentration points, the  $Ti_2Ta_2C_3T_zLi_x$  structures are no longer energetically favorable and further lithium adsorption is unlikely to occur. It is easy to see that lithium ions prefer surface chemistry made of functional groups with smaller atomic masses and higher electronegativity values.  $Ti_2Ta_2C_3O_2Li_x$  systems remain stable with a larger lithium concentration; these results indicate larger lithium intercalation values and, hence, larger energy storage capacities in Li-ion batteries.

Table 6. SFE (eV) of the lithiated MXenes as the lithium concentration increases per formula unit cell.

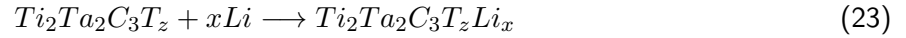
System	SFE (eV) for Li per formula unit cell (x)							
	0.25	0.50	0.50	0.75	1.25	1.50	1.75	2
$Ti_2Ta_2C_3O_2Li_x$	-0.09	-0.03	-0.21	-0.26	-0.20	-0.15	-0.04	0.17
$Ti_2Ta_2C_3F_2Li_x$	-0.03	-0.03	-0.08	-0.09	0.07	-	-	-
$Ti_2Ta_2C_3Cl_2Li_x$	-0.02	0.00	-	-	-	-	-	-
$Ti_2Ta_2C_3(OH)_2Li_x$	-0.00	-	-	-	-	-	-	-

### 5.4.3 Electrochemical characterization: open-circuit voltages

The electrochemical properties of  $Ti_2Ta_2C_3T_zLi_x$  MXenes during the lithiation process were studied using the open-circuit voltage (OCV) as a function of the lithium concentration per unit cell. The OCV of the MXene structures is equal to the negative of its surface formation energy divided by the number of lithium atoms per cell. Let's briefly recall section 4.2.9 with the following equation:

$$OCV = -\frac{\Delta E_f}{x} \quad (22)$$

where  $\Delta E_f$  is the formation energy of the MXene structure and  $x$  is the number of lithium atoms per unit cell. OCV is valuable as it gives important insights into the performance of the MXene structure as an anode material. We considered the following reaction for our calculations:



The OCV curves for all  $Ti_2Ta_2C_3T_zLi_x$  MXenes are shown in figure 14. Positive OCV values are observed for most functionalized  $Ti_2Ta_2C_3T_zLi_x$ , indicating the viability of the MXene material to be used as li-ion battery anode material. Positive OCV values show lithium adsorption into the system, while negative OCV values indicate lithium cluster formation on the surface of the anode material. Maximum lithium capacity is considered when the OCV curve reaches 0 eV; this point can be used to calculate the MXene's theoretical gravimetric capacity (TGC) as follows:

$$Q = \frac{x_{max}zF}{M_{Ti_2Ta_2C_3T_z}} \quad (24)$$

where  $x_{max}$  is the maximum lithium capacity per unit cell,  $z$  is the valence number of the ion (for Li,  $z = 1$ ),  $F$  is the Faraday constant, and  $M_{Ti_2Ta_2C_3T_z}$  is the atomic weight of  $Ti_2Ta_2C_3T_z$ . The TGC's for all  $Ti_2Ta_2C_3T_z$  MXene structures can be seen in table 7 for single and double-sided surfaces.

OH functional groups are to be avoided as they result in negative cell voltage with one lithium per unit cell and thus lower storage capacities. Such behavior has been observed and is in accordance with previous studies (Aierken et al., 2018).

As the lithium concentration increases, the OCV decreases for all functional groups. Lithium ions with concentration values lower than  $x = 1$  are located in the H3 site for  $Ti_2Ta_2C_3O_2Li_x$ ,  $Ti_2Ta_2C_3F_2Li_x$ , and  $Ti_2Ta_2C_3OH_2Li_x$ , while the ions are located in the T4 site for  $Ti_2Ta_2C_3Cl_2Li_x$ . These sites correspond to the most stable high-symmetry site observed for lithium adatoms in each functional group. At larger lithium concentration values ( $x > 1$ ), the lithium ion is located in the second-most stable site, which is T4 for  $Ti_2Ta_2C_3O_2Li_x$  and  $Ti_2Ta_2C_3F_2Li_x$ , and H3 for  $Ti_2Ta_2C_3Cl_2Li_x$ . Slight variations of OCV can be observed in  $Ti_2Ta_2C_3F_2Li_x$ . This slight variance has been observed in pure  $Ti_2Ta_2C_3Li_x$  and  $Ti_4C_3Li_x$  before (Maldonado-Lopez et al., 2022).

The TGC allows us to predict which MXene structure will be the best-performing anode material in Li-ion batteries. The  $x_{max}$  values are 1.8, 1.04, and 0.51 for  $Ti_2Ta_2C_3O_2Li_x$ ,  $Ti_2Ta_2C_3F_2Li_x$ , and

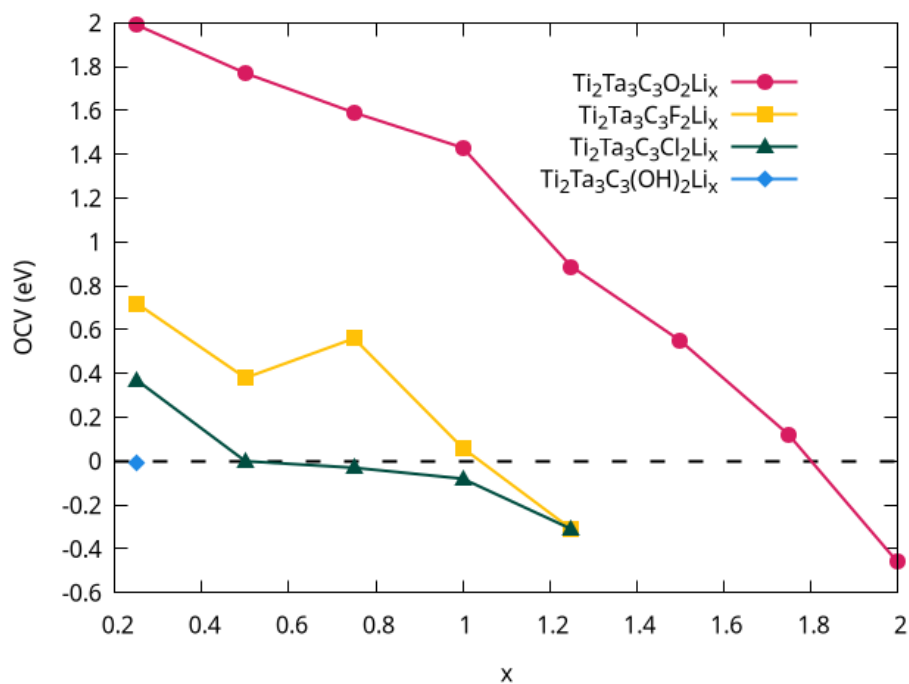


Figure 14. Open circuit voltage curves for the functionalized  $\text{Ti}_2\text{Ta}_2\text{C}_3\text{T}_z$  MXenes. Maximum Li capacity is observed when  $\text{OCV} = 0$ . Positive OCV values show Li intercalation, while negative values indicate surface cluster formation.

Table 7. Theoretical gravimetric capacities calculated from the maximum Li capacity for each MXene anode material.

System		$x_{max}$	$Q(\text{mAh/g})$
$\text{Ti}_2\text{Ta}_2\text{C}_4\text{O}_2\text{Li}_x$	single surface	1.8	91.77
	double surface	3.6	183.55
$\text{Ti}_2\text{Ta}_2\text{C}_4\text{F}_2\text{Li}_x$	single surface	1.04	52.38
	double surface	2.08	104.75
$\text{Ti}_2\text{Ta}_2\text{C}_4\text{Cl}_2\text{Li}_x$	single surface	0.51	24.21
	double surface	1.02	48.42
$\text{Ti}_2\text{Ta}_2\text{C}_4(\text{OH})_2\text{Li}_x$	single surface	-	-
	double surface	-	-

$\text{Ti}_2\text{Ta}_2\text{C}_3\text{Cl}_2\text{Li}_x$ , respectively. Inserting these data points into our TGC gives capacity values of 91.77, 52.38, and 24.21 mAh/g, respectively.  $\text{Ti}_2\text{Ta}_2\text{C}_3\text{O}_2\text{Li}_x$  shows much larger theoretical storage capacities compared to other functionalized  $\text{Ti}_2\text{Ta}_2\text{C}_3\text{T}_z\text{Li}_x$  MXene families. This indicates that  $\text{Ti}_2\text{Ta}_2\text{C}_3\text{O}_2$  MXene anode materials will offer superior storage performance, and therefore, experimental  $\text{Ti}_2\text{Ta}_2\text{C}_3$  synthesis methods for Li-ion battery applications should favor the formation of O functional groups.

#### 5.4.4 Li-ion diffusion paths

To study the Li diffusion process across the surface of the functionalized ordered alloy MXene, we employed the climbing image nudged elastic band method. The minimum energy pathways (MEP) can be observed in Fig. 15 for O and F functional groups. MEP is a useful evaluation to study the charge/discharge cycle of the battery as it gives the energy barriers and saddle points during the Li-ion diffusion process. These results agree with our previous calculations and demonstrate that the H3 site is the most stable configuration for the Li adatom for all functional groups. Models for the Li diffusion process can be seen in figure 16.

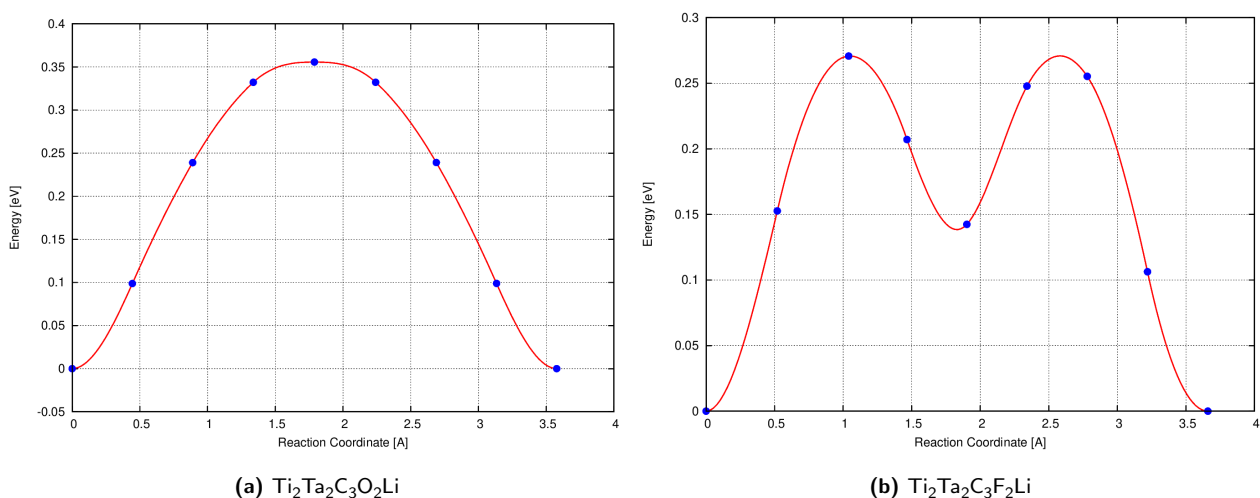


Figure 15. Minimum energy pathways for a)  $\text{Ti}_2\text{Ta}_2\text{C}_3\text{O}_2\text{Li}$  and b)  $\text{Ti}_2\text{Ta}_2\text{C}_3\text{O}_2\text{Li}$ . In the oxidized MXene, the Li adatom travels from H3 to H3 site, with a saddle point at T4 and an energy barrier of around 0.36 eV. In the fluorinated MXene, Li travels from H3 to H3, with a metastable site at T4 (0.28 eV) and saddle points (0.26 eV) at the bridge site.

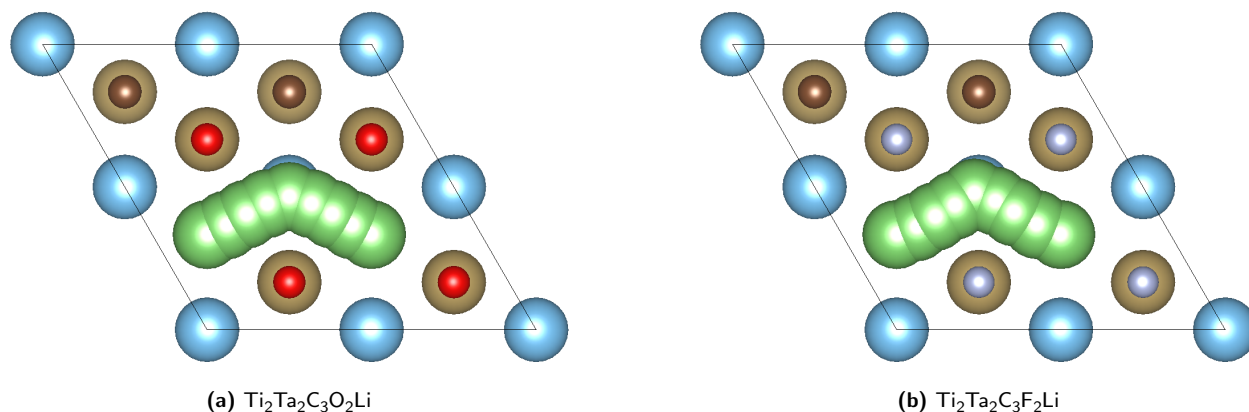


Figure 16. Atomic visual models for the Li diffusion process over the surface of the functionalized MXenes.

For the  $\text{Ti}_2\text{Ta}_2\text{C}_3\text{O}_2$  MXene, the saddle point energy barrier can be found in the T4 site with 355.7 meV.  $\text{Ti}_2\text{Ta}_2\text{C}_3\text{F}_2$  showed differing results; we observe a metastable site at T4 and saddle points in the

bridge site. Its energy barrier was also lower than that of the  $\text{Ti}_2\text{Ta}_2\text{C}_3\text{O}_2$  MXene, showing saddle point energies of 277.8 and 255.3 meV. This indicates that while a  $\text{Ti}_2\text{Ta}_2\text{C}_3\text{O}_2$  anode battery will allow for greater storage capacities, a  $\text{Ti}_2\text{Ta}_2\text{C}_3\text{F}_2$  anode battery will likely allow for faster charge/discharge cycles.

## Chapter 6. Conclusion

---

We employed the VASP software package to study the properties of  $Ti_2Ta_2C_3T_z$  MXenes and its lithiation process. We optimized the structural parameters of the functionalized MXenes and the lithiated structures to find their most stable systems in four high-symmetry sites for the functional groups, as well as four high-symmetry sites for the Li adatom placement. This process was repeated until the MXenes structures were no longer thermodynamically stable. We conclude that the H3 site is the most stable high-symmetry site for  $Ti_2Ta_2C_3O_2$ ,  $Ti_2Ta_2C_3F_2$ ,  $Ti_2Ta_2C_3Cl_2$ ,  $Ti_2Ta_2C_3(OH)_2$ ; all of the functionalized structures are thermodynamically stable systems allowing them to be candidates for anode materials in Li-ion batteries. Additionally, the H3 site was the most stable high-symmetry site for Li adatoms on the MXene surface for  $Ti_2Ta_2C_3O_2$  and  $Ti_2Ta_2C_3F_2$ , while Li adatoms preferred the T4 site in  $Ti_2Ta_2C_3Cl_2$ .

We saturated the surface of the MXenes with Li adatoms until the lithiated systems were no longer thermodynamically stable. This process allowed us to study the electrochemical properties of the MXene materials by employing an open circuit voltage analysis and theoretical gravimetric capacity calculations.  $Ti_2Ta_2C_3O_2$ ,  $Ti_2Ta_2C_3F_2$ ,  $Ti_2Ta_2C_3Cl_2$  exhibit theoretical gravimetric reversible capacities of 91.77, 52.38, and 24.21 mAh/g respectively;  $Ti_2Ta_2C_3(OH)_2$  was not thermodynamically stable upon receiving its first Li adatom. Therefore,  $Ti_2Ta_2C_3O_2$ ,  $Ti_2Ta_2C_3F_2$ , and  $Ti_2Ta_2C_3Cl_2$  are promising materials to be used in Li-ion battery applications. These results demonstrate  $Ti_2Ta_2C_3O_2$  stores more lithium content and thus may allow for larger Li-ion battery storage capacities.

The ion diffusion process was studied using the climbing image nudged elastic band method.  $Ti_2Ta_2C_3O_2$  showed its saddle point at the T4 site with an energy barrier of 355.7 meV. Meanwhile,  $Ti_2Ta_2C_3F_2$  showed a metastable site at T4 and saddle points at the Bridge site with an energy barrier of 277.8 meV. We can gather from these results faster charge/discharge cycles in the fluorinated MXene, hence it may be a more suitable material for application in Li-ion batteries that are not constrained by size and would prefer lower charge times.

## References

- Aghamohammadi, H., Eslami-Farsani, R., & Castillo-Martinez, E. (2022). Recent trends in the development of MXenes and MXene-based composites as anode materials for Li-ion batteries. *Journal of Energy Storage*, 47. <https://doi.org/10.1016/J.EST.2021.103572>.
- Aierken, Y., Sevik, C., Gülseren, O., Peeters, F. M., & Çakır, D. (2018). Mxenes/graphene heterostructures for li battery applications: a first principles study. *Journal of Materials Chemistry A*, 6(5), 2337–2345. <https://doi.org/10.1039/C7TA09001C>.
- Barsoum, M. W. (2000). MN+1AXN phases: a new class of solids; thermodynamically stable nanolaminates. *Progress in Solid State Chemistry*, 28, 201. [https://doi.org/10.1016/S0079-6786\(00\)00006-6](https://doi.org/10.1016/S0079-6786(00)00006-6).
- Cho, J., Jeong, S., & Kim, Y. (2015). Commercial and research battery technologies for electrical energy storage applications. *Progress in Energy and Combustion Science*, 48, 84–101. <https://doi.org/10.1016/J.PECS.2015.01.002>.
- Deng, D. (2015). Li-ion batteries: basics, progress, and challenges. *Energy Science & Engineering*, 3(5), 385–418. <https://doi.org/10.1002/ese3.95>.
- Eklund, P., Palmquist, J.-P., Höwing, J., Trinh, D., El-Raghy, T., Högberg, H., & Hultman, L. (2007). Ta<sub>4</sub>alc<sub>3</sub>: Phase determination, polymorphism and deformation. *Acta materialia*, 55(14), 4723–4729. <https://doi.org/10.1016/j.actamat.2007.04.040>.
- Energy Storage Association (2022). Batteries. <http://energystorageassociationarchive.org/why-energy-storage/technologies/solid-electrode-batteries/>.
- Er, D., Li, J., Naguib, M., Gogotsi, Y., & Shenoy, V. B. (2014). Ti<sub>3</sub>C<sub>2</sub> mxene as a high capacity electrode material for metal (li, na, k, ca) ion batteries. *ACS applied materials & interfaces*, 6(14), 11173–11179. <https://doi.org/10.1021/am501144q>.
- García-Romeral, N., Morales-Garcia, A., Viñes, F., de PR Moreira, I., & Illas, F. (2023). How does thickness affect magnetic coupling on ti-based mxenes. *Physical Chemistry Chemical Physics*. <https://doi.org/10.1039/D3CP01617J>.
- Grimme, S., Antony, J., Ehrlich, S., & Krieg, H. (2010). A consistent and accurate ab initio parametrization of density functional dispersion correction (dft-d) for the 94 elements h-pu. *The Journal of chemical physics*, 132(15). <https://doi.org/10.1063/1.3382344>.
- Henkelman, G., Uberuaga, B. P., & Jónsson, H. (2000). A climbing image nudged elastic band method for finding saddle points and minimum energy paths. *The Journal of chemical physics*, 113(22), 9901–9904. <https://doi.org/10.1063/1.1329672>.
- Hu, T., Mei, X., Wang, Y., Weng, X., Liang, R., & Wei, M. (2019). Two-dimensional nanomaterials: fascinating materials in biomedical field. *Science Bulletin*, 64(22), 1707–1727. <https://doi.org/10.1016/J.SCIB.2019.09.021>.
- International Energy Agency (2021). Global Energy Review 2021. <https://www.iea.org/reports/global-energy-review-2021>.
- Ivchenko, V. I., Lesnaya, M. I., Nemchenko, V. F., & Kosolapova, T. Y. (1976). Some physical properties of ternary compounds in the system Ti-Al-C. *Soviet Powder Metallurgy and Metal Ceramics*, 15(5), 367–369. <https://doi.org/10.1007/BF00806472>.

- Julien, C., Mauger, A., Vijn, A., & Zaghbi, K. (2015). Lithium Batteries: Science and Technology. *Lithium Batteries: Science and Technology*, 1–619. <https://doi.org/10.1007/978-3-319-19108-9>.
- Kurtoglu, M., Naguib, M., Gogotsi, Y., & Barsoum, M. W. (2012). First principles study of two-dimensional early transition metal carbides. *Mrs Communications*, 2, 133–137. <https://doi.org/10.1557/mrc.2012.25>.
- Lee, J. G. (2016). *Computational materials science: an introduction*. CRC press. <https://www.routledge.com/Computational-Materials-Science-An-Introduction-Second-Edition/Lee/p/book/9781498749732>.
- Li, X., Huang, Z., Shuck, C. E., Liang, G., Gogotsi, Y., & Zhi, C. (2022). MXene chemistry, electrochemistry and energy storage applications. *Nature Reviews Chemistry* 2022, 1–16. <https://doi.org/10.1038/s41570-022-00384-8>.
- Liang, Y., Zhao, C. Z., Yuan, H., Chen, Y., Zhang, W., Huang, J. Q., Yu, D., Liu, Y., Titirici, M. M., Chueh, Y. L., Yu, H., & Zhang, Q. (2019). A review of rechargeable batteries for portable electronic devices. *InfoMat*, 1(1), 6–32. <https://doi.org/10.1002/INF2.12000>.
- Liu, J. & Xue, D. (2010). Hollow Nanostructured Anode Materials for Li-Ion Batteries. *Nanoscale Research Letters*, 5, 1525–1534. <https://doi.org/10.1007/s11671-010-9728-5>.
- Lochala, J. A., Zhang, H., Wang, Y., Okolo, O., Li, X., Xiao, J., Lochala, J. A., Wang Okolo, Y. O., Xiao, J., Zhang, H., & Li, X. (2017). Practical Challenges in Employing Graphene for Lithium-Ion Batteries and Beyond. *Small Methods*, 1(6). <https://doi.org/10.1002/smt.201700099>.
- Maldonado-Lopez, D., Rodriguez, J. R., Pol, V. G., Syamsai, R., Andrews, N. G., Gutiérrez-Ojeda, S. J., Ponce-Pérez, R., Moreno-Armenta, M. G., & Guerrero-Sánchez, J. (2022). Atomic-Scale Understanding of Li Storage Processes in the Ti<sub>4</sub>C<sub>3</sub> and Chemically Ordered Ti<sub>2</sub>Ta<sub>2</sub>C<sub>3</sub> MXenes: A Theoretical and Experimental Assessment. 12, 25. <https://doi.org/10.1021/acsaem.1c03239>.
- Martins, V. L., Neves, H. R., Monje, I. E., Leite, M. M., De Oliveira, P. F., Antoniassi, R. M., Chauque, S., Morais, W. G., Melo, E. C., Obana, T. T., Souza, B. L., & Torresi, R. M. (2020). An Overview on the Development of Electrochemical Capacitors and Batteries – Part I. *Anais da Academia Brasileira de Ciências*, 92(2), 1–28. <https://doi.org/10.1590/0001-3765202020200796>.
- Meyer, J. C., Geim, A. K., Katsnelson, M. I., Novoselov, K. S., Booth, T. J., & Roth, . S. (2007). The structure of suspended graphene sheets. 446. <https://doi.org/10.1038/nature05545>.
- Miao, Y., Hynan, P., Von Jouanne, A., & Yokochi, A. (2019). Current Li-Ion Battery Technologies in Electric Vehicles and Opportunities for Advancements. <https://doi.org/10.3390/en12061074>.
- Momma, K. & Izumi, F. (2011). Vesta 3 for three-dimensional visualization of crystal, volumetric and morphology data. *Journal of applied crystallography*, 44(6), 1272–1276. <https://doi.org/10.1107/S0021889811038970>.
- Naguib, M., Kurtoglu, M., Presser, V., Lu, J., Niu, J., Heon, M., Hultman, L., Gogotsi, Y., & Barsoum, M. W. (2011). Two-dimensional nanocrystals produced by exfoliation of Ti<sub>3</sub>AlC<sub>2</sub>. *Advanced Materials*, 23(37), 4248–4253. <https://doi.org/10.1002/adma.201102306>.
- Perdew, J. P., Burke, K., & Ernzerhof, M. (1996). Generalized Gradient Approximation Made Simple. *Physical Review Letters*, 77(18), 3865. <https://doi.org/10.1103/PhysRevLett.77.3865>.

- Poulomi, R. & Srivastava, S. K. (2014). Nanostructured Anode Materials for Lithium Ion Batteries. *Journal of Materials Chemistry A*, (6). <https://doi.org/10.1039/C4TA04980B>.
- Qian, G.-X., Martin, R. M., & Chadi, D. (1988). First-principles study of the atomic reconstructions and energies of Ga- and As-stabilized GaAs (100) surfaces. *Physical Review B*, 38(11), 7649. <https://doi.org/10.1103/PhysRevB.38.7649>.
- Roselin, L. S., Juang, R. S., Hsieh, C. T., Sagadevan, S., Umar, A., Selvin, R., & Hegazy, H. H. (2019). Recent advances and perspectives of carbon-based nanostructures as anode materials for Li-ion batteries. *Materials*, 12(8). <https://doi.org/10.3390/ma12081229>.
- Secretaría de Energía (2016). Prospectiva de Energías Renovables 2012-2016. [https://www.gob.mx/cms/uploads/attachment/file/62954/Prospectiva\\_de\\_Energ\\_as\\_Renovables\\_2012-2026.pdf](https://www.gob.mx/cms/uploads/attachment/file/62954/Prospectiva_de_Energ_as_Renovables_2012-2026.pdf).
- Shein, I. & Ivanovskii, A. (2012). Graphene-like titanium carbides and nitrides  $\text{TiN}_x$ ,  $\text{TiC}_x$  ( $x=1, 2, \text{ and } 3$ ) from de-intercalated MAX phases: First-principles probing of their structural, electronic properties and relative stability. *Computational Materials Science*, 65, 104–114. <https://doi.org/10.1016/j.commatsci.2012.07.011>.
- Stram, B. N. (2016). Key challenges to expanding renewable energy. *Energy Policy*, 96(September 2016), 728–734. <https://doi.org/10.1016/J.ENPOL.2016.05.034>.
- Subsecretaría de Planeación y Transición Energética (2020). Balance Nacional de Energía 2020. Secretaría de Energía. [https://www.gob.mx/cms/uploads/attachment/file/707654/BALANCE\\_NACIONAL\\_ENERGIA\\_0403.pdf](https://www.gob.mx/cms/uploads/attachment/file/707654/BALANCE_NACIONAL_ENERGIA_0403.pdf).
- Sun, S., Liao, C., Hafez, A. M., Zhu, H., & Wu, S. (2018). Two-dimensional MXenes for energy storage. *Chemical Engineering Journal*, 338, 27–45. <https://doi.org/10.1016/J.CEJ.2017.12.155>.
- Sun, W., Shah, S. A., Chen, Y., Tan, Z., Gao, H., Habib, T., Radovic, M., & Green, M. J. (2017). Electrochemical etching of  $\text{Ti}_2\text{AlC}$  to  $\text{Ti}_2\text{CT}_x$  (MXene) in low-concentration hydrochloric acid solution. *Journal of Materials Chemistry A*, 5(41), 21663–21668. <https://doi.org/10.1039/c7ta05574a>.
- Syamsai, R., Rodriguez, J. R., Pol, V. G., Van Le, Q., Batoo, K. M., Farooq, S. A., Pandiaraj, S., Muthumareeswaran, M. R., Raslan, E. H., & Grace, A. N. (2021). Double transition metal MXene ( $\text{Ti}_x\text{Ta}_{4-x}\text{C}_3$ ) 2D materials as anodes for Li-ion batteries. *Scientific Reports*, 11(1). <https://doi.org/10.1038/S41598-020-79991-8>.
- Tan, K. M., Babu, T. S., Ramachandramurthy, V. K., Kasinathan, P., Solanki, S. G., & Raveendran, S. K. (2021). Empowering smart grid: A comprehensive review of energy storage technology and application with renewable energy integration. *Journal of Energy Storage*, 39. <https://doi.org/10.1016/J.EST.2021.102591>.
- Tarascon, J. M. & Armand, M. (2001). Issues and challenges facing rechargeable lithium batteries. *Nature*, 414(6861), 359–367. <https://doi.org/10.1038/35104644>.
- U.S. Energy Information Administration (2021). International Energy Outlook 2021. U.S. Department of Energy, Washington, DC. [https://www.eia.gov/outlooks/ieo/pdf/IEO2021\\_Narrative.pdf](https://www.eia.gov/outlooks/ieo/pdf/IEO2021_Narrative.pdf).
- Wang, V., Xu, N., Liu, J.-C., Tang, G., & Geng, W.-T. (2021). Vaspkit: A user-friendly interface facilitating high-throughput computing and analysis using vasp code. *Computer Physics Communications*, 267, 108033. <https://doi.org/10.1016/j.cpc.2021.108033>.
- Zhu, F., Liu, G., Tao, C., Wang, K., & Jiang, K. (2017). Battery management system for Li-ion battery. *The Journal of Engineering*. <https://doi.org/10.1049/joe.2017.0569>.